

Cite this article as:

Gurreri, L., Tamburini, A., Cipollina, A., Micale, G., Ciofalo, M., CFD prediction of concentration polarization phenomena in spacer-filled channels for Reverse Electrodialysis, *Journal of Membrane Science*, 468 (2014) 133–148  
<http://dx.doi.org/10.1016/j.memsci.2014.05.058>

## **CFD prediction of concentration polarization phenomena in spacer-filled channels for Reverse Electrodialysis**

**L. Gurreri<sup>a</sup>, A. Tamburini<sup>a</sup>, A. Cipollina<sup>a</sup>, G. Micale<sup>a\*</sup>, M. Ciofalo<sup>b</sup>**

<sup>a</sup> *Dipartimento di Ingegneria Chimica, Gestionale, Informatica, Meccanica*

<sup>b</sup> *Dipartimento dell'Energia, Ingegneria dell'Informazione e Modelli Matematici*

*Università di Palermo, Viale delle Scienze Ed. 6, 90128 Palermo (ITALY);*

\* Corresponding author: [giorgiod.maria.micale@unipa.it](mailto:giorgiod.maria.micale@unipa.it)

### **Abstract**

Salinity Gradient Power generation through Reverse Electrodialysis (SGP-RE) is a promising technology to convert the chemical potential difference of a salinity gradient into electric energy. In SGP-RE systems, as in most membrane processes, concentration polarization phenomena may affect the theoretical driving force and thus the performance of the process. Operating conditions, including the feed solution flow rate and concentration and the channels' geometrical configuration, may greatly influence both the polarization effect and the pumping energy consumption. The present work uses CFD to investigate the dependence of concentration polarization and pressure drop on flow rate, feeds concentration, current density and spacer features. Concentration polarization effects were found to be significant at low feed solution concentration (river water), but only secondary at higher concentrations (seawater and brine), thus suggesting that different optimization strategies should be employed depending on the feeds concentration. The features that a spacer-filled channel should possess for high efficiency and high current density SGP-RE applications were identified.

Keywords

CFD, Reverse Electrodialysis, concentration polarization, spacer-filled channel, mixing promoter.

## 1 Introduction

Salinity Gradient Power by Reverse Electrodialysis (SGP-RE) is a technology to draw electric energy from the mixing of solutions at different salt concentrations. In particular, SGP-RE allows the production of electricity harvesting energy from the difference in chemical potential between two saline solutions flowing in alternate channels separated by selective ion exchange membranes (IEMs) [1]. A stack contains several repeating units (*cell pairs*), each consisting of a cationic exchange membrane (CEM), a compartment fed by a more concentrated salt solution (e.g. seawater), an anionic exchange membrane (AEM) and a compartment fed by a more dilute salt solution (e.g. river water). Spacers are usually employed in order to (i) separate the membranes, thus creating the channels and (ii) promote fluid mixing. The chemical potential difference between the two salt solutions generates an ion transport from the concentrated solution towards the dilute one in each cell pair: cations move selectively through the CEMs and anions through the AEMs, towards the cathode and the anode, respectively. At the electrodes, the ionic transport is converted by redox reactions into a current of electrons supplying an external load. Continuity of the electrochemical potential through the system causes the chemical potential difference to generate an electric potential difference across each membrane. The sum of the voltages generated over all the membranes is the overall difference of electrical potential available at the electrodes (Open Circuit Voltage). A schematic representation of a SGP-RE stack is reported in Figure 1; more details can be found in the literature [1-4].

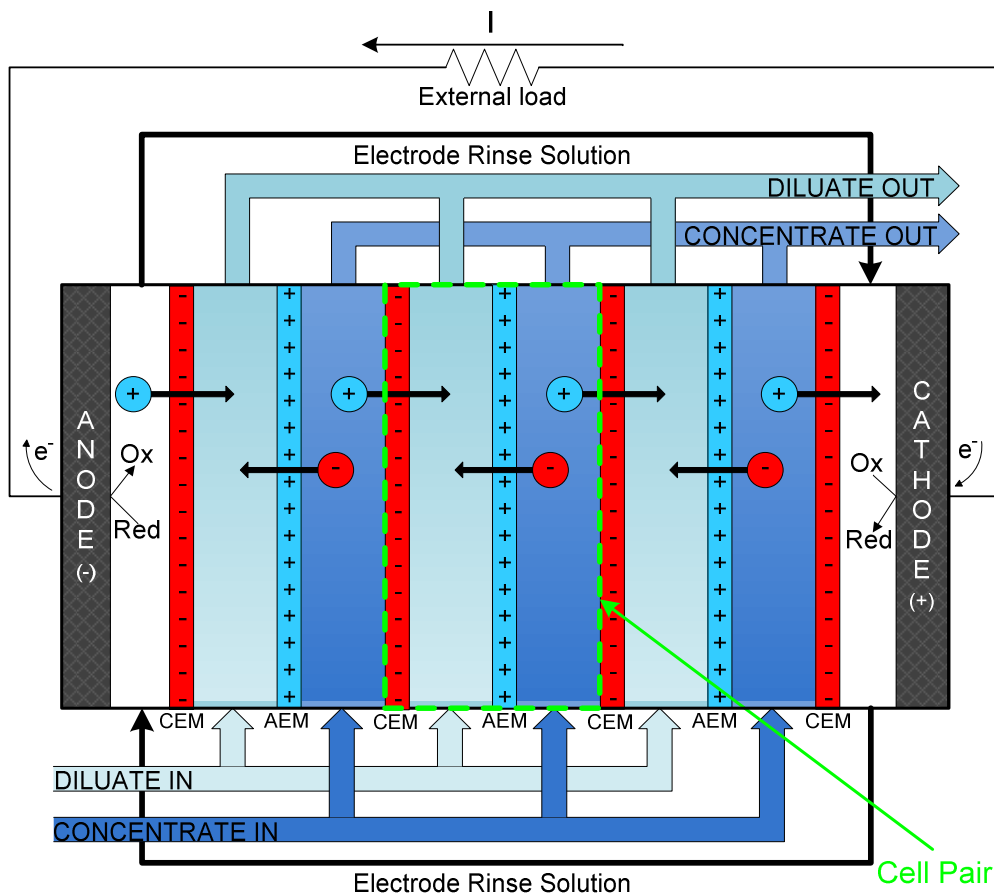


**Figure 1.** Schematic representation of a Reverse Electrodialysis stack. The sketch highlights one cell pair including the spacer filled channel investigated.

Many factors affect the performance of this process [2, 5-8]: properties of components such as membranes, spacers and electrodic systems, but also stack geometry, operating conditions and feed properties. Fluid dynamics influences crucial quantities affecting the process performance, i.e. pressure drop and concentration polarization. Polarization phenomena are well known to affect the efficiency of membrane separation processes by reducing the theoretical driving force [9-15]: the mass flux through the ion exchange membranes, accompanied by a difference between ions mobility in the membrane and solution phases, gives rise to concentration gradients in the boundary layer between the membrane surface and the well mixed bulk [16]. In Reverse Electrodialysis, concentration polarization phenomena result in an increased salt concentration at the membrane surface in the dilute channel and a decreased salt concentration at the membrane surface in the

concentrate channel. As a consequence, the concentration difference at the membrane-solution interfaces becomes smaller than the concentration difference between the bulk solutions, the resulting electromotive force becomes lower than the theoretical value, and a lower voltage over the stack is obtained [8].

Potential drops due to boundary layer effects are usually divided by the electric current in order to obtain a “non-Ohmic resistance” which can be compared with the corresponding Ohmic resistance within the channel. The Ohmic and non-Ohmic contributions can be measured by chronopotentiometry. Post et al. [3] employed this technique for the case of a stack provided with spacer-filled channels either 0.5 mm or 0.2 mm thick, concluding that the stack resistance was mainly Ohmic, but a non-Ohmic resistance of 6% and 16% respectively was also present. Increasing the current density with the aim of enhancing target power densities may lead to a stronger effect of non-Ohmic resistances on process performance. According to Vermaas et al. [8], the non-Ohmic resistance should be divided into two different contributions, one related to the concentration polarization phenomenon ( $R_{BL}$ ), the other to the change of the bulk concentration along the fluid flow ( $R_{AC}$ ). By applying chronopotentiometry technique, the authors measured  $R_{BL}$  and found that it can be reduced by increasing the fluid velocity and thus the mixing efficiency. Also, a small intermembrane distance along with a finer spacer mesh was found to reduce  $R_{BL}$ . Brauns [17] proposed to use corrugated membranes instead of the more common net spacers; stacks with such membranes were tested by Vermaas et al. [18] and exhibited a significantly lower Ohmic resistance, but a distinctively higher boundary layer resistance with respect to the classical net spacer stacks. Vermaas et al. [19] proposed a method to predict  $R_{BL}$  from design parameters only: they assumed that the degree of mixing in the boundary layers depends on the velocity shear at the membrane-solution interface. Długolecki et al. [20] employed direct current measurements coupled with electrochemical impedance spectroscopy in order to measure all the contributions to the

resistance across an IEM: pure membrane resistance, diffusion boundary layer resistance and double layer resistance. Experimental data revealed that, at very low salt concentration (0.017M NaCl), the dominant resistance is the diffusion boundary layer resistance, while the other two contributions are of minor importance. At higher salt concentration (0.5M NaCl), the pure membrane resistance is the dominant one, the diffusion boundary layer plays a considerable role and the double layer resistance is not significant. Also, from a previous work presented by Długolecki et al. [21] it appears that, at low flow rates: (i) concentration polarization phenomena account for the dominant resistance and (ii) the so called “spacer shadow” effect (a contribution to the Ohmic resistance) is significant.

Summarizing, concentration polarization may considerably affect the actual membrane potential, thus reducing the gross power produced; but the magnitude of the concentration polarization in the boundary layer and its relevance to the process performance depend on the feed solution flow rate and concentration and on the cell and spacer geometry.

Published computational studies of transport phenomena in channels for Reverse Electrodialysis are only few. Brauns [17] used the Lacey [22] approach, based on a simplified concentration polarization layer model, to evaluate the effect of various parameters on electrical power output. Recently, the same author refined the analysis by using two-dimensional finite element modelling [23]; the steady state salt ion flux through the membranes and the corresponding ion concentration distribution within the solution compartments were investigated. No attempts have been specifically devoted so far to the 3D CFD prediction of concentration polarization phenomena.

Almost all information available so far on transport phenomena in RE units concerns cases in which seawater and river water are used as feed solutions, while few studies [23, 24] have been devoted to the case of brine and seawater (*BS*). This combination is currently being investigated within the EU-

FP7 funded REAPower project [25-27] as a possible effective alternative to the traditional one (seawater – river water, *SR*), in which the dilute channel resistance is very high.

In the present work, a CFD model is developed by means of the finite volume code Ansys-CFX 13. For the first time, (i) a CFD model based on the Stephan Maxwell equation is employed to deal with ion transport in Reverse Electrodialysis channels; (ii) a fully predictive numerical simulation based on the Unit Cell approach is devised for the modelling of ion concentration transport; (iii) different spacer-channel configurations, including the poorly studied ones involving spacers with woven filaments, are investigated. The aim of this study is to assess concentration polarization. This analysis provides insight into the mass transfer phenomena in SGP-RE, where an optimisation of channel geometry and operating conditions is crucial for efficiency and economic competitiveness. The influence of parameters as flow rate, feed concentration (brine, seawater and river water), molar flux through the membranes (i.e. current density) and spacer configuration is evaluated.

## **2 CFD modelling**

### *2.1 Systems under investigation*

Different configurations of Reverse Electrodialysis channels were investigated:

- i) channels equipped with four different spacers (see Figure 2): (A) a diamond spacer 400  $\mu\text{m}$  thick made by woven filaments, supplied by Fumatech; (B) an ideal diamond spacer 400  $\mu\text{m}$  thick with the same sizes, but made by overlapped filaments; (C) a coarser diamond spacer with thickness of 508  $\mu\text{m}$  and overlapped filaments, supplied by DelStar (Naltex); and (D) a spacer with woven filaments and thickness of 280  $\mu\text{m}$ , supplied by Deukum;
- ii) an empty (i.e. spacerless) channel (E) with a thickness of 400  $\mu\text{m}$ .

Since industrial or large-scale prototype SGP-RE plants do not yet exist, commercial spacers purposely manufactured for this application are not available. All the above spacers are produced for different membrane-based processes (Direct Electrodialysis, Osmosis etc.) or for general purposes (e.g. packaging), and – in lack of more specific spacers – have been adopted by most groups which currently conduct experimental work on SGP-RE [5-8] as an alternative to profiled membranes [18]. All the spacers analysed here are similar, apart from the smaller scale (implying lower operational Reynolds numbers), to those used in Membrane Distillation (MD), on which our group is currently conducting both experimental [13, 14] and computational work.

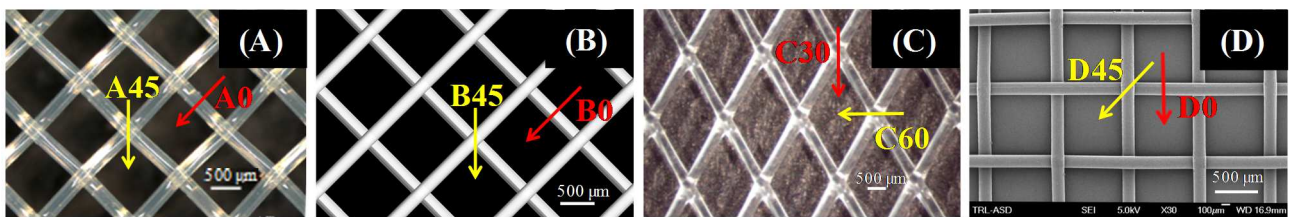


**Figure 2.** Commercial spacers supplied by (A) Fumatech, (C) DelStar (Naltex) and (D) Deukum. (B) is an ideal spacer studied for comparison purposes which does not exist physically. Arrows indicate the different flow directions with respect to the spacer that were investigated.

Geometric characterization work, based on optical microscopy and thickness measurements by a micrometer, was performed for the three physical spacers in order accurately to reproduce the same geometries in the numerical simulations.

Table 1 summarizes the geometric features of all the spacers investigated, showing also the angle between the main flow direction and the filaments assumed in the simulations. For each spacer two different angles were investigated, as indicated in Figure 2 by red and yellow arrows. For the spacers with perpendicular filaments, i.e. Fumatech (A), Deukum (D) and the ideal spacer (B), the flow direction is either parallel to a filament or bisects the angle formed by the filaments; for the DelStar Naltex spacer (C) the flow direction bisects either of the angles formed by the filaments.

For convenience, hereafter the test cases studied will be indicated by a letter followed by a number; the letter identifies the spacer (A, B, C or D) while the number specifies the flow incidence angle.

**Table 1.** Geometric features of the spacers investigated and angle between the flow direction and a filament.

Spacer	Configuration	Supplier/ Manufacturer	Filament arrangement	Thickness [ $\mu\text{m}$ ]	Filament diameter [ $\mu\text{m}$ ]	Mesh length [ $\mu\text{m}$ ]	Volume porosity [-]	Angle between filaments [ $^\circ$ ]	Angle between flow direction and a filament [ $^\circ$ ]
A	A0	Fumatech	Woven	400	210	1100	0.84	90	0
	A45								45
B	B0	(ideal)	Overlapped	400	210	1100	0.84	90	0
	B45								45
C	C30	DelStar Naltex	Overlapped	508	312	1960	0.83	60-120	30
	C60								60
D	D0	Deukum	Woven	280	148	809	0.85	90	0
	D45								45

In the proximity of the contact points between the filaments, either a compenetration (overlapped design) or a compression (woven design) of filaments can be observed. Similarly, compression issues occur in the contact areas between spacer and membranes. These geometrical features were somewhat taken into account during the generation of the geometry for the CFD simulations; in particular, the filament diameter was assumed equal to that measured via optical microscopy photographs, and the difference between twice the filament diameter and the spacer thickness was attributed 70% to the overlap region of the filaments and 30% to the filament-membrane contacts.

Different NaCl feed solutions at 25°C were simulated: Feed1 at a concentration equal to 5M, Feed2 at 0.5M and Feed3 at 0.017M, representing nearly saturated brine, seawater and river water, respectively. The density and viscosity of the solutions were obtained from Green and Perry [28] and Ozbek et al. [29]. The diffusivity of NaCl in aqueous solutions was derived from Vitagliano and Lyons [30]. Table 2 summarizes the physical properties of the NaCl solutions.

**Table 2.** Physical properties of NaCl aqueous solutions at 25°C.

Solution	Molarity [mol/l]	Density [kg/m <sup>3</sup> ]	Viscosity [Pa s]	NaCl diffusivity [m <sup>2</sup> /s]
Feed1 (brine)	5.0	1183	1.66·10 <sup>-3</sup>	1.580·10 <sup>-9</sup>
Feed2 (seawater)	0.5	1017	9.31·10 <sup>-4</sup>	1.472·10 <sup>-9</sup>
Feed3 (river water)	0.017	998	8.91·10 <sup>-4</sup>	1.533·10 <sup>-9</sup>

## 2.2 Governing equations

### 2.2.1 Continuity and momentum equations

The governing equations for three-dimensional flow of a Newtonian incompressible fluid are the following continuity and Navier-Stokes equations:

$$\vec{\nabla} \cdot \vec{u} = 0 \quad (1)$$

$$\rho \frac{\partial \vec{u}}{\partial t} + \rho \vec{u} \vec{\nabla} \cdot \vec{u} = -\vec{\nabla} p + \mu \nabla^2 \vec{u} \quad (2)$$

where  $\vec{u}$  is velocity,  $\rho$  is density,  $\mu$  is dynamic viscosity and  $p$  is pressure. Laminar steady state simulations were performed as the flow was predicted to be steady at all the flow rates investigated on the basis of preliminary time-dependent simulations.

The density was assumed to be constant since its changes associated with concentration gradients along both the streamwise and the cross-stream directions were estimated to be very small. For the same reason, buoyancy due to concentration gradients was neglected.

### 2.2.2 Transport equation in concentrated solutions

When highly concentrated solutions are employed, the approach based on the Nernst-Planck equation [31] should not be used, since it is strictly valid only for dilute solutions. A more rigorous approach was proposed by Newman [31], who derived the following electrolyte transport equation from the Stefan-Maxwell equations under the assumptions of (i) binary electrolyte and (ii) local electroneutrality (implying conservation of charge,  $\vec{\nabla} \cdot \vec{i} = 0$ ):

$$\frac{\partial C}{\partial t} + \vec{\nabla} \cdot (C\vec{u}_0) = \vec{\nabla} \cdot \left[ D \left( 1 - \frac{d \ln C_0}{d \ln C} \right) \vec{\nabla} C \right] - \frac{\vec{i} \cdot \vec{\nabla} t_i^0}{z_i \nu_i F} \quad (3)$$

In eq. (3)  $C$  is the electrolyte concentration,  $C_0$  is the solvent concentration,  $\vec{u}_0$  is the solvent velocity (identified here with the solution velocity  $\vec{u}$ ),  $D$  is the diffusion coefficient of the salt,  $\vec{i}$  is the current density,  $t_i^0$  is the transport number with respect to the solvent velocity,  $z_i$  is the valence ( $=\pm 1$  for NaCl),  $\nu_i$  is the stoichiometric coefficient of ionic species  $i$  ( $=1$  for NaCl), and  $F$  is the Faraday constant. Subscript  $i$  refers to either cation or anion. Eq. (3) includes four terms: the first and second on the left hand side are the transient and advection term, respectively, while the first on the right hand side is the diffusive term. The last term on the right hand side (migrative term) coincides, taking account of the charge conservation condition expressed by  $\vec{\nabla} \cdot \vec{i} = 0$ , with the divergence of the migrative flux of either species and is nonzero only if either transport number exhibits a spatial gradient. Note that different transport numbers for the two ionic species imply different fluxes, but not different concentrations: since electroneutrality is assumed, concentrations of  $\text{Na}^+$  and  $\text{Cl}^-$  are everywhere the same. For the sake of simplicity, in the present work the additional assumption of equal transport numbers for the two species was also made.

The implementation and the solution of eq. (3) along with suitable initial and boundary conditions allow the distribution of the variable  $C$  to be obtained within the computational domain.

Since a CFD simulation cannot deal with phenomena occurring in the electric double layer at the membrane interface (i.e. at the molecular scale) or within the membrane itself, the present modelling procedure cannot directly simulate these features and takes account of them by imposing an electrolyte flux at the fluid-membrane interface as a boundary condition. Thus, the aim of the present CFD modelling is the assessment of local concentration polarization phenomena occurring at a far larger scale than that of the electric double layer.

With respect to an ordinary transport equation, eq. (3) exhibits two sources of additional difficulty: (i) the effective diffusion coefficient varies with concentration, and (ii) a source term containing the current density appears at the right hand side.

(i) As regards the former difficulty, it has been demonstrated [31] that:

$$1 - \frac{d \ln C_0}{d \ln C} = \frac{\rho - C \frac{d\rho}{dC}}{\rho - C \cdot M_e} \quad (4)$$

where  $M_e$  is the molar mass of the solute. By locally linearizing  $\rho(C)$  as

$$\rho = a \cdot C + b \quad (5)$$

the following simple expression is obtained

$$1 - \frac{d \ln C_0}{d \ln C} = \frac{b}{b + (a - M_e) \cdot C} \quad (6)$$

The parameters  $a$  and  $b$  were obtained *via* linear regression of the function  $\rho = \rho(C)$  [28] in the proximity of the bulk concentration of each of the three solutions to be simulated (5M Feed1, 0.5M Feed2 and 0.017M Feed3). Therefore, three couples of values were employed for the parameters  $a$  and  $b$  as reported in Table 3.

**Table 3.** Values of parameters  $a$  and  $b$  for the three feeds.

Feed	$a$ [kg/mol]	$b$ [kg/m]
Feed1 (5 M brine)	0.03493	1008.808
Feed2 (0.5M seawater)	0.03986	997.327
Feed3 (0.017M river water)	0.04127	997.000

The inconsistency between treating  $\rho$  as a constant in eqs. (1)-(2) and as a function of  $C$  in eq. (5) is only apparent: eq. (5) serves the purpose of computing the derivative  $d\rho/dC$  which appears at the right hand side of eq. (4) and is necessary to express the diffusivity correction in the Newman transport equation. On the other hand, if variations of  $C$  across the channel are small (as it is the case here), variations of  $\rho$  (and  $\mu$ ) are negligible from the hydrodynamic point of view.

(ii) As regards the latter difficulty, solving eq. (3) in its complete form, which contains the current density  $\vec{i}$ , would require either an additional equation for this quantity or an *a priori* knowledge of its distribution. The latter situation occurs only in the case of a spacerless channel, where the current density can be assumed to be uniform. Thus, simulations were first carried out in a spacerless channel 400  $\mu\text{m}$  thick, in order to quantify the relative importance of the last term in eq. (3) (migrative term) with respect to the diffusive one (of course, in the empty channel no convective contributions are present in the direction orthogonal to the membranes). The dependence of the transport number on the concentration was derived from Smits and Duyvis [32]. Figure 3 reports the  $\text{Na}^+$  transport number as a function of the NaCl concentration, showing a weak dependence.

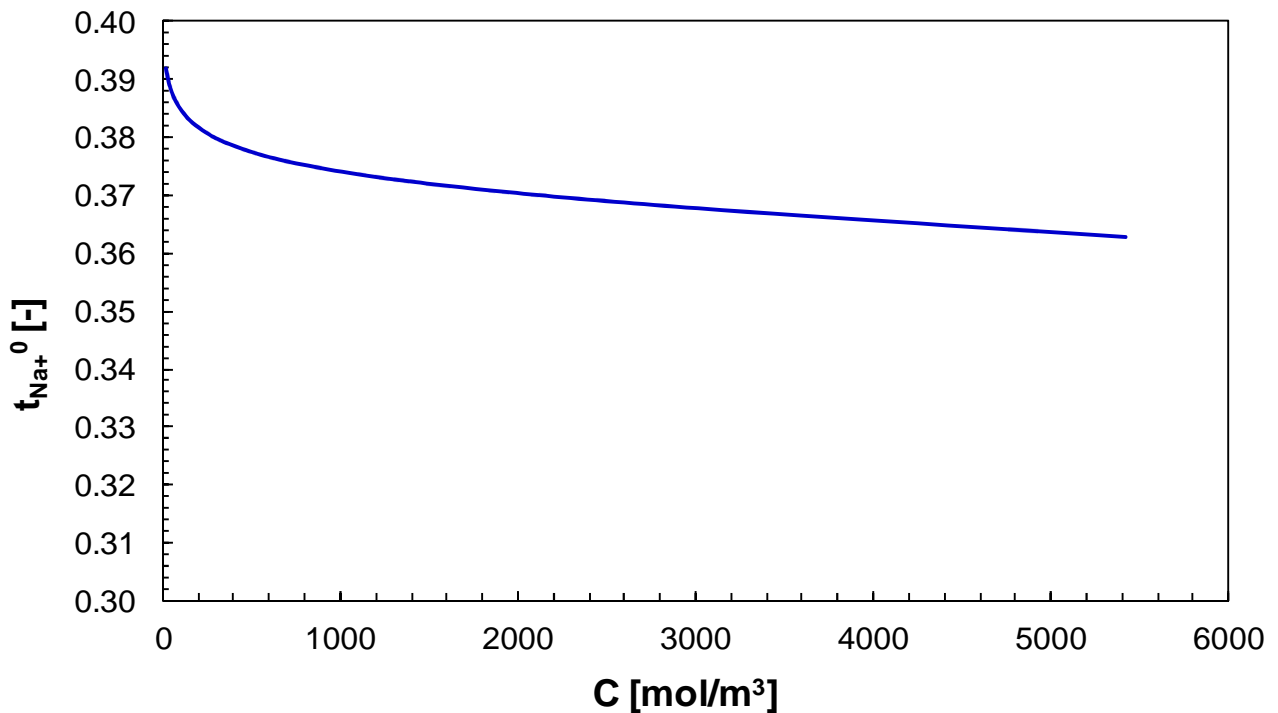


**Figure 3.** Transport number of the sodium ion in NaCl solutions at 25°C [32].

Results showed that the concentration profiles obtained by CFD simulations taking into account the migrative term are practically coincident with those obtained by neglecting it. This evidence is reported in Figure 4a for the most unfavourable case (low concentration and high current density), where the migrative term was found to be negligible compared to the diffusive one (Figure 4b).

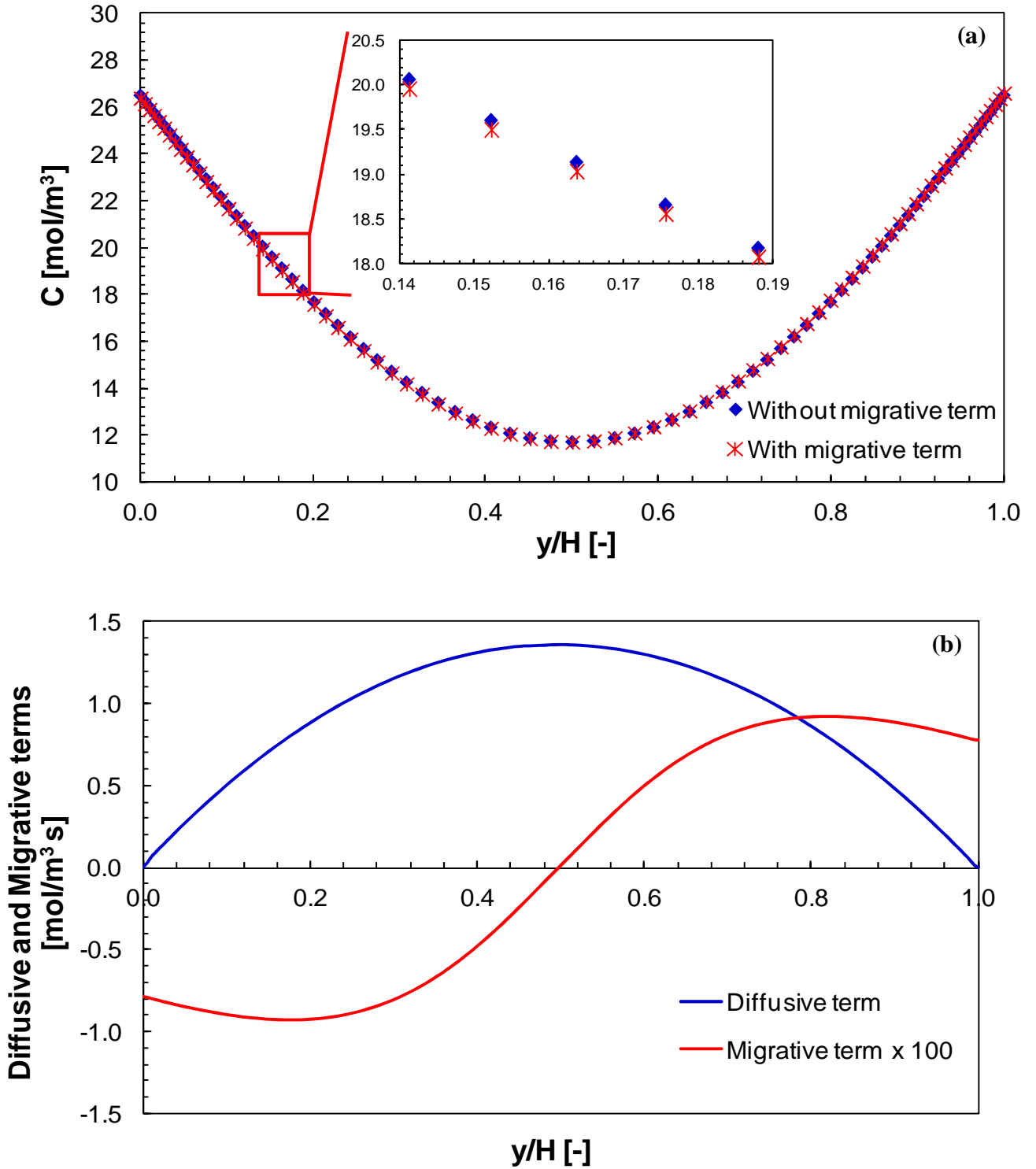


**Figure 4.** Assessment of the contribution of transport equation's migrative and diffusive terms along a monitoring line perpendicular to the membranes for the case of the empty channel fed by Feed3 at  $w_{ave} = 1.5$  cm/s and  $i = 35$  A/m<sup>2</sup>. (a) Electrolyte concentration profiles obtained with or without the migrative term; (b) comparison of the contributions of the diffusive and the migrative term. Here,  $y/H$  represents the  $y$ -coordinate normalized by the channel thickness  $H$ .

We stress once more that these findings do not mean that the migrative *flux* is negligible, but only that its *divergence* is negligible. Taking the above results into account, CFD simulations were carried out by neglecting the last term in eq. (3) and using eq. (6) to model the diffusivity correction. Therefore, the equation solved in the CFD simulations is:

$$\vec{\nabla} \cdot (C\vec{u}_0) = \vec{\nabla} \cdot \left[ D \frac{b}{b + (a - M_e)C} \vec{\nabla} C \right] \quad (7)$$

Eq. (7) is similar to a standard convection-diffusion transport equation apart from the corrective term which accounts for the dependence of diffusivity on electrolyte concentration.

### 2.3 Computational domain and boundary conditions

Only one channel was simulated in each CFD simulation, i.e. either the concentrated or the dilute channel, depending on the feed solution concentration (brine always feeds a concentrated channel, while river water always feeds a dilute channel).

In order to avoid excessive computational requirements, the Unit Cell approach was adopted. It is widely employed in the literature [7, 33-36] and consists of simulating a periodic repetitive unit representative of the region of the spacer-filled channel far from inlet, outlet and side boundaries, in which fully developed flow and concentration fields can be assumed.

On the basis of the geometric characterization of the spacers, the computational domains (Unit Cells) were defined as shown in Figure 5. The choice of the cell orientation with respect to the spacer wires is largely arbitrary, and is suggested by ease of computational domain build-up. In order to simplify the notation, in each case the computational domain was rotated with respect to the reference frame  $Oxyz$  so that the main flow direction coincided with the  $z$  axis. For uniformity, the same Unit Cell sizes were adopted for the empty channel (not shown in the figure) as for the A and B spacer-filled channels.

The computational domain was discretized by either hexahedral grids for the case of the empty channel or hybrid (hexahedral-tetrahedral) grids for the case of the spacer-filled channels. The use of hybrid meshes was made necessary by the geometrical complexities of the spacer wires, which are difficult to be meshed by hexahedra only. However, such grids are mainly composed by hexahedral volumes: parallelepipeds were built around each filament and discretized with tetrahedra while the rest of the computational domain was discretized by mapped hexahedral volumes [7, 24, 37]. Hexahedral or hybrid grids provide a greater accuracy for a given number of degrees of freedom and a better convergence to grid-independent results with respect to fully tetrahedral grids. The sensitivity of the results to the discretization degree was carefully tested: both local and global quantities (e.g. the average velocity in the whole domain) were compared as functions of the number of computational volumes for the case of the highest velocity investigated. For the Unit Cells, the grids employed in the present work exhibited a maximum discrepancy with the finest grid (at least 3 times finer) lower than 2%, thus guaranteeing the practical independence of the results on the discretization degree. Details of the hybrid meshes in one half of a cross section are reported in the insets of Figure 5.

The mesh features are summarized in Table 4, which also reports the number of control volumes comprised in the channel height  $H$  (the number of volumes along a filament diameter is one half of this). Table 4 includes also the case of an empty channel.

**Table 4.** Summary of the grids employed.

Unit Cell	Number of cells in height $H$	Number of cells	% of volume discretized with hexahedral cells
Empty channel	37	~50'000	100
A	22	~500'000	76.0
B	26	~500'000	94.3
C	23	~800'000	78.2
D	28	~1'600'000	76.1

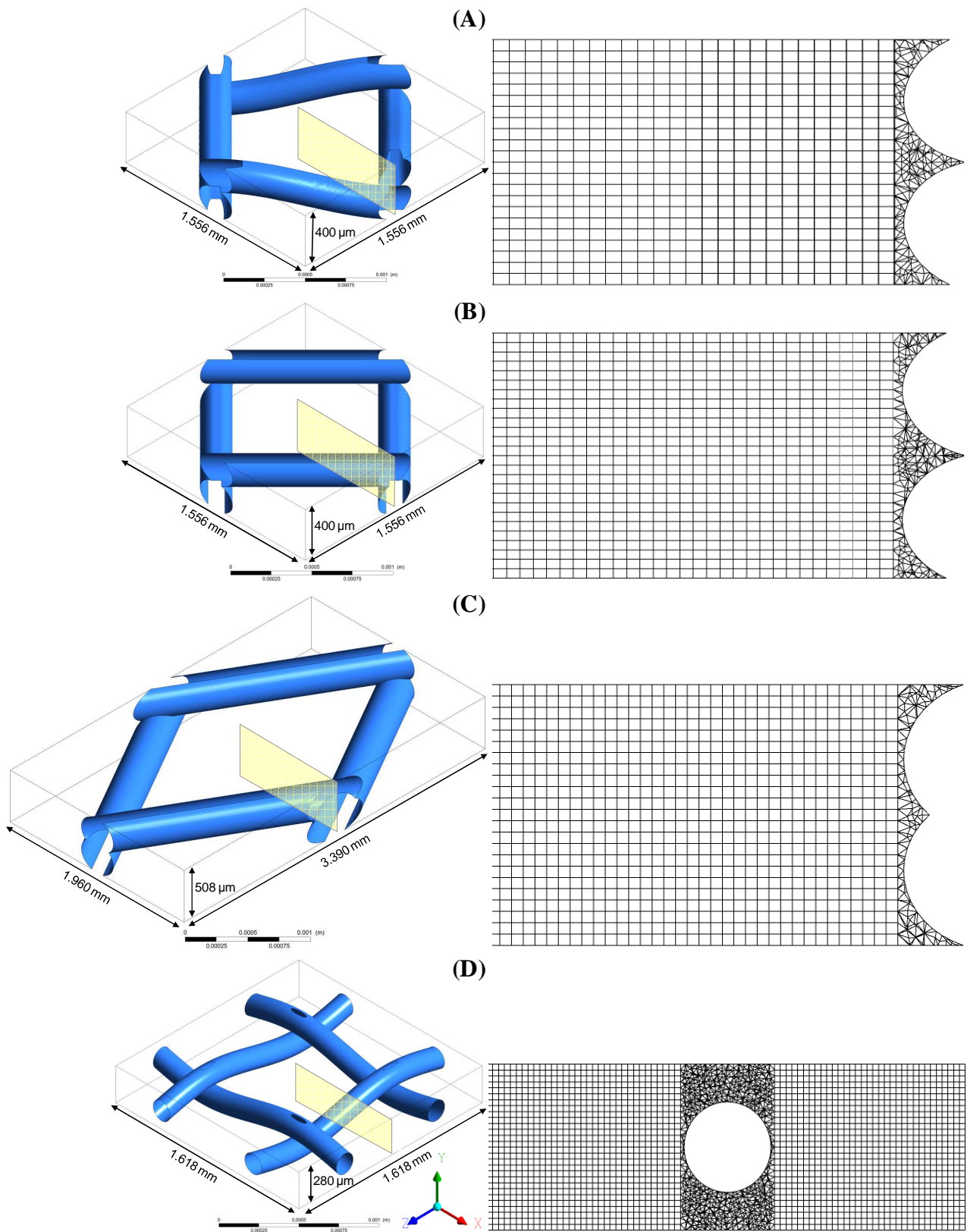


**Figure 5.** Unit Cell geometry for channels filled with spacers (A) through (D). Insets show details of the mesh over one half of a cross section.

Fluid flow velocities ranging from 0.1 to 14.3 cm/s were investigated, on the basis of typical residence time and pressure drop constraints on the flow velocities in RE channels. Corresponding values of the Reynolds numbers ranged from  $\sim 1$  to  $\sim 125$ ; following Schock and Miquel [38],  $Re$  was defined as:

$$Re = \frac{\rho w_{mean,void} d_{h,void}}{\mu} \quad (8)$$

where  $w_{mean,void}$  is the average velocity along the main flow direction  $z$  in a corresponding spacer-less channel, and the hydraulic diameter of the spacer-less channel is twice the channel thickness

$$d_{h,void} = 2H \quad (9)$$

#### 2.4 Boundary conditions for membrane modelling

The upper and lower surfaces of the domain represent the membrane-solution interfaces. Outgoing or incoming fluxes of the electrolyte were imposed on these walls as discussed below, according to whether the computational domain represents the concentrated or the dilute channel, respectively. From the hydrodynamic point of view, they were treated as impermeable walls with ordinary no slip boundary conditions; this simplifying assumption is coherent with the general assumption of one-way coupling between flow and concentration fields and is justified by the fact that, under the conditions analyzed here, the electrolyte flux in or out of the membrane walls in a single Unit Cell can be estimated never to exceed  $10^{-4}$  times the mass flow rate crossing the same cell. Spacer filament surfaces were considered as walls with no slip and no flux boundary conditions.

Since the equation solved is eq. (7), in which only convection and diffusion are explicitly accounted for, the boundary conditions to be set at the fluid-membrane interfaces must involve only diffusive fluxes. Migrative fluxes are not explicitly described by the model because they do not enter concentration balances, but can be deduced from the diffusive ones as described below.

First, note that current density, transport number and migrative flux in the solution in contact with the IEM are related to one another through the following expression

$$\vec{J}_i^m = \frac{t_i^0}{z_i F} \vec{i} \quad (10)$$

where  $\vec{J}_i^m$  is the migrative flux of species  $i$ . By regarding the membranes as ideal (i.e., with permselectivity  $\alpha = 1$ ) the total flux of the co-ion at the membrane-solution interface must be zero. As an example, a cationic exchange membrane is shown in Figure 6. Here, it is the total flux of Cl<sup>-</sup> at the membrane-solution interface that can be assumed to be zero ( $\vec{J}_{-,CEM}^{tot} = 0$ ). As a consequence, the diffusive and the migrative fluxes of the co-ion must be equal and opposite, and the diffusive flux of co-ion can be written as:

$$\vec{J}_{co,IEM}^d = -\frac{t_{co}^0}{z_{co} F} \vec{i} \quad (11)$$

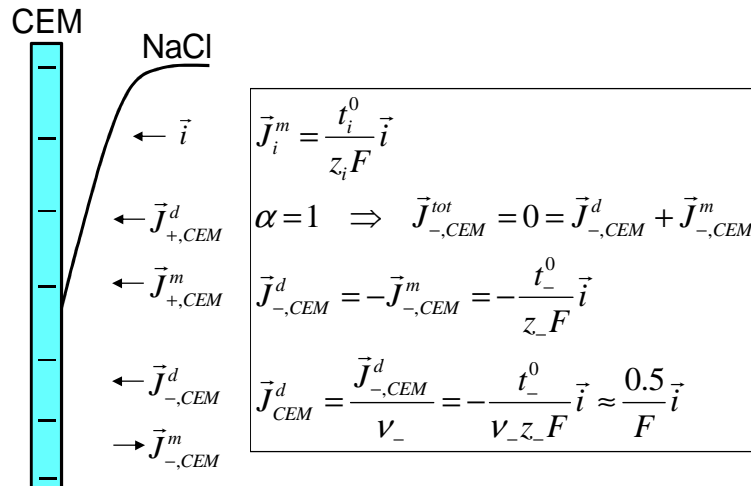


**Figure 6.** Ionic fluxes near the cationic exchange membrane within the concentrated channel, showing the link between diffusive flux and current density.

Taking into account the local electroneutrality condition, the diffusive flux of the electrolyte is

$$\vec{J}^d = \vec{J}_i^d / \nu_i, \text{ and at the membrane-solution interfaces it can be expressed from eq. (11) as}$$

$$\vec{J}_{IEM}^d = -\frac{t_{co}^0}{\nu_{co} z_{co} F} \vec{i} \quad (12)$$

Clearly, for monovalent binary electrolytes such as NaCl, the diffusive fluxes of Na<sup>+</sup>, Cl<sup>-</sup> and electrolyte are the same ( $\nu_+ = \nu_- = 1$ ,  $z_+ = -z_- = 1$ ).

For NaCl, the transport numbers of cation and anion are slightly different ( $t_+^0 \approx 0.4$ ;  $t_-^0 \approx 0.6$ ). Explicitly accounting for this would lead to two different fluxes to be set on the two membranes, resulting in a larger concentration polarization on one of the membranes and a lower polarization on the opposite one, with related difficulties in the definition of a single polarization coefficient. Here we assumed for simplicity the transport properties of Na<sup>+</sup> and Cl<sup>-</sup> to be the same within the solution, so that the corresponding fluxes can be considered equal and a single concentration polarization can be defined. As pointed out by a reviewer, the assumption of equal transport numbers would be more closely satisfied by different electrolytes, e.g. KCl, suggesting that their use would be recommendable in experiments designed to measure polarization.

Note that the assumption of equal transport properties, together with that of negligible gradients of transport numbers, implies that predicted concentration profiles are independent of migration. Eq. (12) allows a suitable diffusive boundary condition  $\vec{J}_{IEM}^d$  to be deduced from a known current density. A homogeneous flux of electrolyte was imposed. According to the above remarks and to eq. (12), the value implemented was computed from the current density as

$$J_{IEM}^d = \pm \frac{i \cdot 0.5}{F} \quad (13)$$

An incoming flux is considered positive (dilute channel), while an outgoing one is considered negative (concentrated channel).

Since eq. (7) includes a concentration-dependent diffusivity, the flux is not linearly dependent on the concentration gradient. Therefore, it may be interesting to carry out simulations at different

current densities (i.e. different fluxes). “High” or “low” current densities can be defined with respect to the maximum current density that would be attainable in the absence of non-Ohmic (i.e. concentration-related) losses. For each electrolyte couple, this is a short circuit current, whose assessment requires estimates for (i) the maximum (open circuit) potential associated with that couple (e.g. *BS* or *SR*); (ii) the overall Ohmic resistance of the electrolyte-filled channels; (iii) the Ohmic resistance of the membranes. While estimate (i) can be made with good accuracy, estimates (ii) and (iii) require simplifying assumptions and can only be approximate. Here, we assumed the coupled channels to have the same thickness, neglected the influence of the spacer (which increases the Ohmic resistance of the channel with respect to a void one) and used realistic values for the membrane resistance. Care was taken that, for any given electrolyte couple considered, the value chosen for the current density in the simulations was sufficiently lower than this maximum value. For example, in their SGP-RE tests, Tedesco et al. [39] measured values of about  $3.7 \times 10^{-4} \Omega \text{m}^2$  for the sum of the Ohmic resistances of anionic and cationic membranes. In twin D-type spacer-filled channels ( $H = 280 \mu\text{m}$ ) the short circuit current density would be  $237 \text{ A/m}^2$  for brine-seawater (*BS*,  $E_{OCV} = 0.105 \text{ V}$ ) and  $82 \text{ A/m}^2$  for seawater-river water (*SR*,  $E_{OCV} = 0.153 \text{ V}$ ). Of course, higher current densities will be possible if lower-resistance membranes will become available. When different electrolyte couples were compared, as in Figure 10 and Figure 11, the highest current density was limited by the more dilute of the couples (i.e. *SR*, seawater-river water) which is why only values up to  $60 \text{ A/m}^2$  were considered.

Concentration polarization phenomena are usually quantified via polarization factors, defined as the ratio between the bulk and membrane-solution interface concentration. In formulae:

$$\theta^{conc} = \frac{\bar{C}_w^{conc}}{\hat{C}_b^{conc}} \text{ for concentrated channel (brine)} \quad (14)$$

$$\theta^{dil} = \frac{\hat{C}_b^{dil}}{\bar{C}_w^{dil}} \text{ for diluted channels (seawater and river water)} \quad (15)$$

where  $\bar{C}_w$  is the mean concentration at the membrane-solution interface and  $\hat{C}_b$  is the bulk concentration, defined as the mass flow weighted average of the concentration on a cross section of the Unit Cell (e.g. a  $x$ - $y$  plane). According to the above definition,  $\theta$  is always lower than 1, and the higher the  $\theta$  value, the less significant the polarization effects.

## 2.5 Treatment of periodicity

In the Unit Cell approach periodic boundary conditions are imposed to all variables between the inlet and outlet faces. On the other hand, it is necessary to allow for a streamwise variation of (i) pressure (due to frictional losses) and (ii) bulk concentration (due to solute inflow or outflow through the channel walls). This apparent contradiction is managed as follows.

(i) Consider first the hydrodynamic issue, involving pressure. In the fully-developed region of a channel, the static pressure  $p$  can be split by definition into a periodic component  $\tilde{p}$ , whose spatial distribution repeats itself identically in each Unit Cell, and a large-scale component  $-K_p z$  which decreases linearly along the main flow direction  $z$  with a gradient  $K_p = |dp/dz|$ . By substituting  $\tilde{p} - K_p z$  for  $p$  in the Navier-Stokes eq. (2), it is easy to recognize that it can be written as

$$\rho \frac{\partial \vec{u}}{\partial t} + \rho \vec{u} \vec{\nabla} \cdot \vec{u} = -\vec{\nabla} \tilde{p} + \mu \nabla^2 \vec{u} + K_p \vec{k} \quad (16)$$

in which  $\vec{k}$  is the unit vector of the  $z$  axis. Eq. (16) is similar to eq. (2) but (i) a body force per unit volume (mean pressure gradient) acting along the flow direction  $z$  was added to the right hand side,

and (ii) the “true” pressure  $p$  was replaced by its periodic component  $\tilde{p}$ . If required, the “true” static pressure  $p$  can always be reconstructed from the simulation results as  $p = \tilde{p} - K_p z$ . Note that the pressure gradient  $K_p = |dp/dz|$  is imposed as a known constant, while the flow velocity is computed as a result; this is equivalent to imposing not the bulk Reynolds number in eq. (8) but the friction Reynolds number which, for a plane channel, can be defined as  $Re_{\tau} = u_{\tau}(H/2)/(\mu/\rho)$ , with  $u_{\tau} = (\tau/\rho)^{1/2}$  (friction velocity) and  $\tau = (H/2)|dp/dz|$  (mean wall shear stress).

(ii) A similar treatment is adopted for the concentration  $C$ . By definition of fully developed conditions,  $C$  can be split into a periodic component  $\tilde{C}$  and a large-scale component  $K_c z$ , where the gradient  $K_c = (dC/dz)$  can now be either positive (net inflow of electrolyte into the channel) or negative (net outflow of electrolyte from the channel). By substituting  $\tilde{C} + K_c z$  for  $C$  in eq. (7), after some manipulation the following transport equation is obtained:

$$\bar{\nabla}(\tilde{C}\tilde{u}_0) = \bar{\nabla}\left[D\frac{b}{b+(a-M_e)(\tilde{C}+K_c z)}\bar{\nabla}\tilde{C}\right] - K_c w \quad (17)$$

The last term at the right hand side is implemented in the code as a source term

$$S = -K_c w = -\frac{\bar{J}_{IEM}^d A}{V} \frac{w}{w_{ave}} \quad (18)$$

in which  $\bar{J}_{IEM}^d$  is the mean value of the electrolyte flux at walls (imposed in the simulation),  $A$  is the membrane surface area in a Unit Cell and  $V$  is its volume. The quantity  $\bar{J}_{IEM}^d A/V$  is the mean value of the source term, while  $w/w_{ave}$  represents a local correction.

The approach described for the simulation of fully developed conditions has been widely adopted by the authors in previous work involving heat or mass transport [33]. Apart from numerical approximations, it guarantees solute mass conservation: the mean value of the bulk concentration

(in the proper sense of mass-flow weighted average of  $C$  in a cross section) adopted as the initial guess is conserved through the simulation.

## 2.6 Numerical details

The finite volume code Ansys®-CFX 13 was employed to discretize and solve the former equations. The High Resolution scheme was used for the discretization of the convective terms and shape functions were used to evaluate spatial derivatives for all the diffusion terms. A coupled algorithm was adopted to solve for pressure and velocity. A different number of iterations, depending on flow rate, system geometry etc., were used for the present steady state simulations.

## 3 Results and discussion

The influence of several process parameters on concentration polarization phenomena was investigated: feed solution concentration, fluid velocity and current density. Detailed results relevant to a specific configuration (D0) will be presented and discussed first in section 3.1, while a comparison between the polarization performances of all the configurations investigated will be presented in section 3.2, focusing on the effects of spacer geometry and orientation.

### 3.1 Influence of feed concentration, velocity and current density on polarization phenomena

An example of the concentration field is reported in Figure 7 for the case of the diluted channel fed by Feed3 (0.017M river water) in a D0 spacer-filled channel, a case purposely chosen the better to visualize polarization phenomena. The quantity shown is the “true” (non periodic) concentration, i.e.  $C = \tilde{C} + K_c z$ . Different planes are considered: (a) an  $x$ - $z$  plane located midway between the two membranes, (b)  $y$ - $z$  planes, (c)  $x$ - $y$  planes and (d) the planes representing membrane-solution

interfaces (walls).

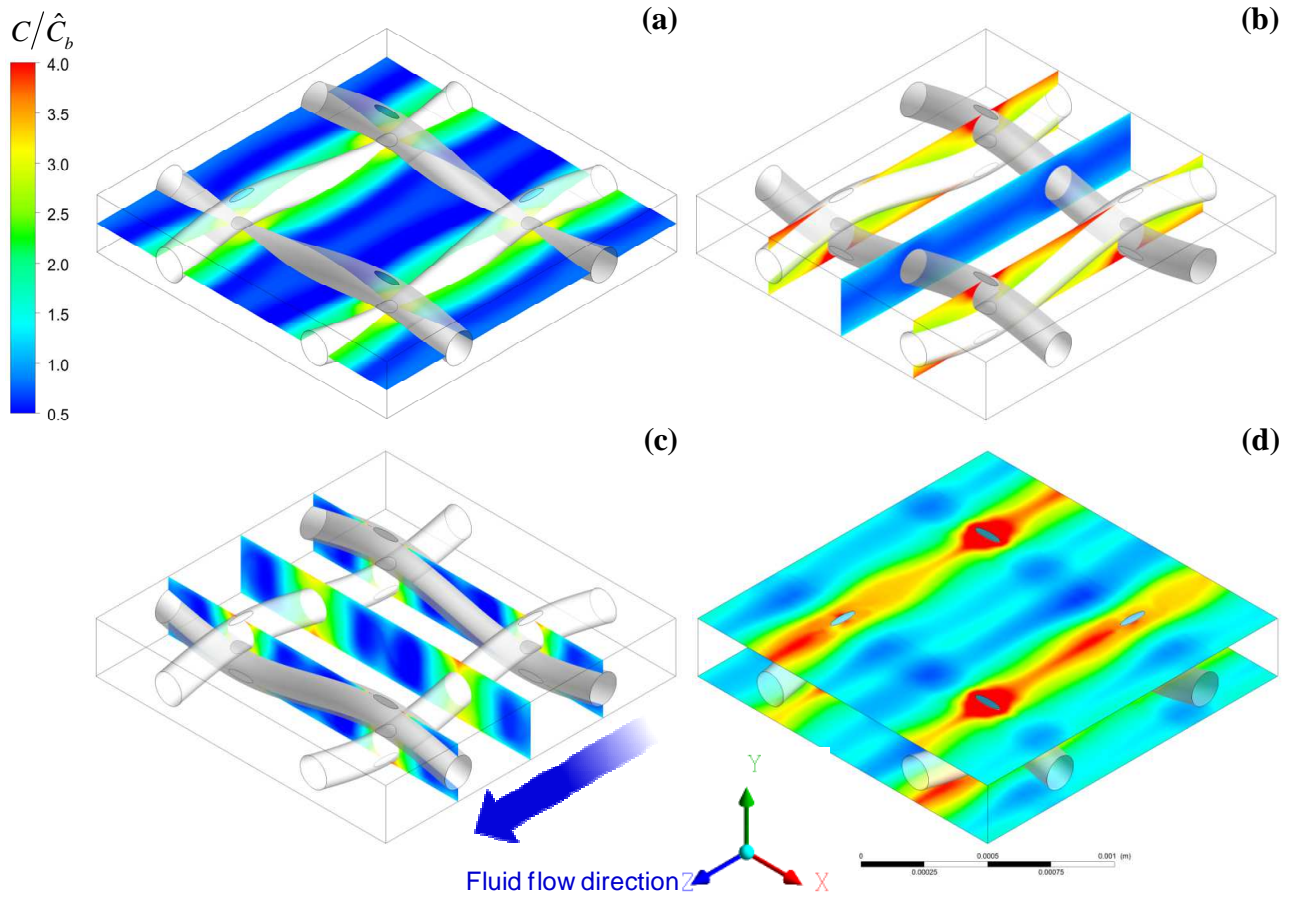


**Figure 7.** Normalized concentration maps on (a)  $x$ - $z$  midplane, (b)  $y$ - $z$  planes, (c)  $x$ - $y$  planes and (d) membrane-solution interfaces for the D0 spacer-filled channel fed by Feed3 (0.017M river water) at  $w_{ave} = 1.53$  cm/s ( $Re = 8$ ),  $i = 60$  A/m<sup>2</sup>.

The figure shows that (i) the presence of the spacer affects the concentration field, (ii) the change of concentration along the main flow direction is negligible, and (iii) the variation of concentration between the central part of the channel and the fluid-membrane interfaces is prominent (i.e., high concentration polarization): compare, for example, the midplane distribution in graph (a) with the wall distribution in graph (d).

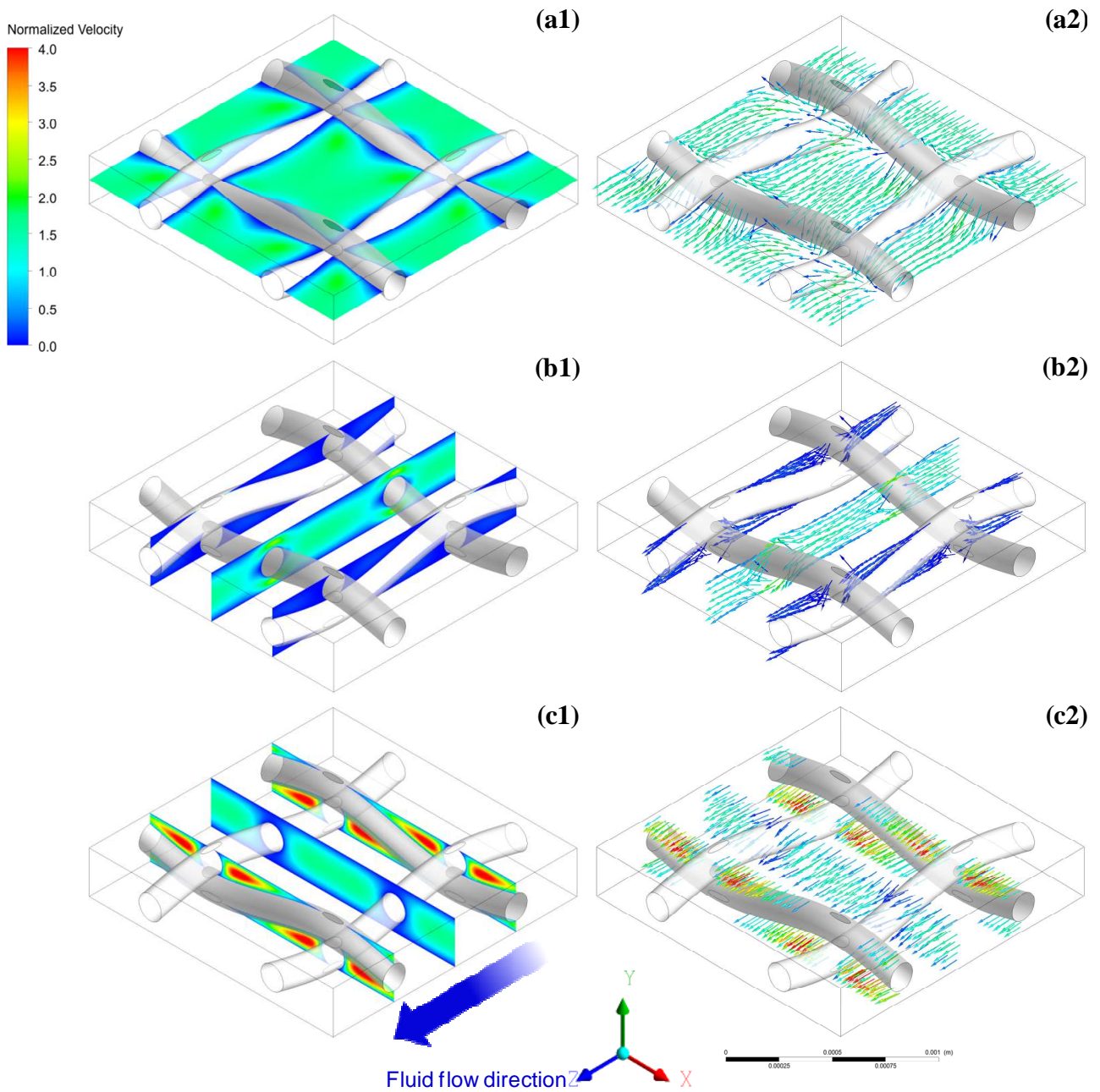


**Figure 8.** Normalized velocity maps and corresponding vector plots on (a)  $x$ - $z$  midplane, (b)  $y$ - $z$  planes and (c)  $x$ - $y$  planes for the D0 spacer-filled channel at  $w_{ave} = 1.53$  cm/s ( $Re = 8$ ).

Velocity maps and vector plots on the same planes of Figure 7 are reported in Figure 8. As it can be seen, the presence of the spacer wires reduces the section for the passage of the fluid thus resulting in a local increase of the velocity (Figure 8-c1). Conversely, low velocity gradients can be observed far from the filaments and domain boundaries in accordance with the low Reynolds number laminar flow regime. Velocity vector plots show that velocity components perpendicular to the membranes

are present near the filaments orthogonal to the main fluid flow direction (Figure 8-a2,b2). Low velocities with no components perpendicular to the membrane are observed near the longitudinal filaments, thus resulting in the maximum polarization areas (Figure 8d). Velocity vector plots of Figure 8-a2,b2 indicate a symmetric flow field without any fluid detachment downstream of the orthogonal filaments, thus confirming the existence of a creeping flow regime.

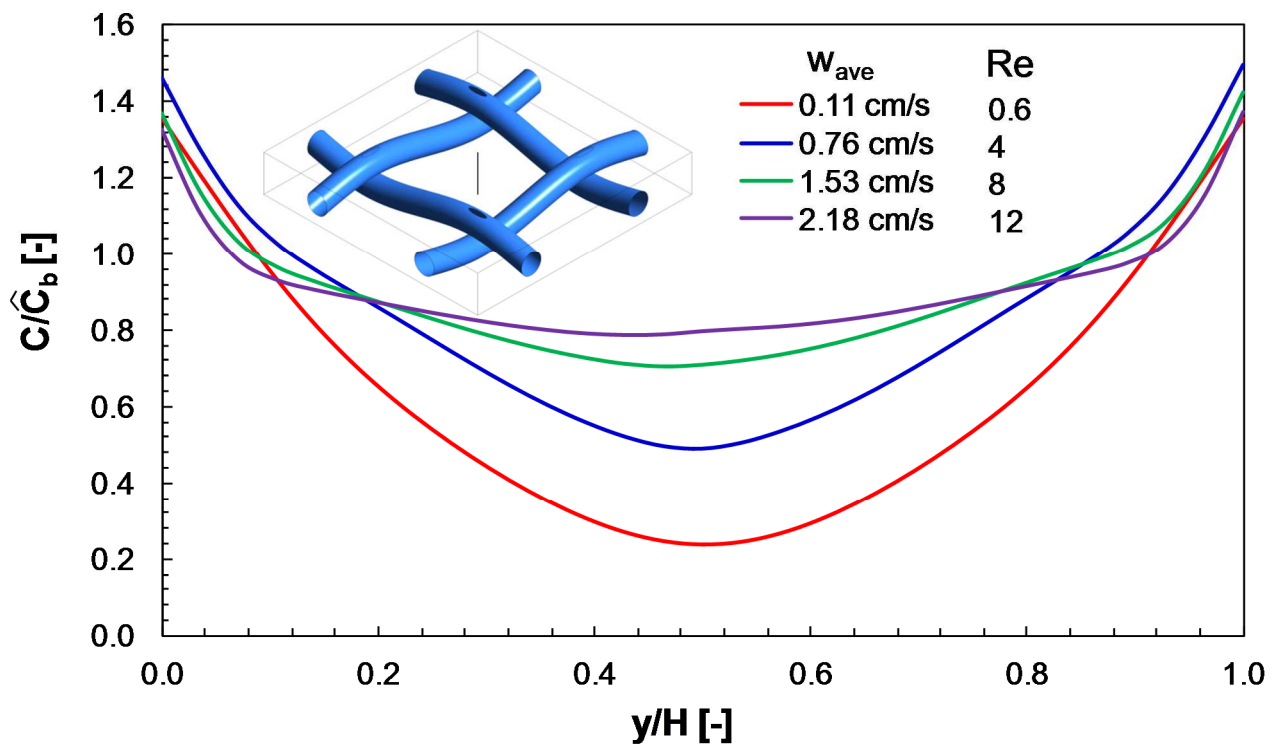


**Figure 9.** Normalized electrolyte concentration profiles along a monitoring line perpendicular to the membranes and placed in the centre of the cell for the case of the D0 spacer-filled channel fed by Feed3 (0.017M river water) at various mean flow velocities and  $i = 60A/m^2$ . Here,  $y/H$  represents the  $y$ -coordinate normalized by the channel thickness  $H$ .

Polarization depends on both mean and local velocities. A first example of the effect of fluid velocity on concentration polarization is provided by Figure 9, where the normalized concentration profiles along a line perpendicular to the membranes and placed in the centre of the Unit Cell are shown at different mean fluid velocities. As expected, the mixing enhancement due to the increasing Reynolds number tends to reduce concentration gradients between bulk and membranes.

Figure 10 reports the mass transfer coefficient (defined as the ratio between the diffusive flux at the

membrane-solution interface,  $J_{IEM}^d$ , and the wall – to – bulk concentration difference,  $\bar{C}_w - \hat{C}_b$ ) as a function of the mean fluid velocity  $w_{ave}$  for the three feeds. The figure shows that this quantity increases significantly with the flow rate. The fact that the curves at various current densities (and thus at various fluxes) are practically identical means that the non-linearity of the transport equation (due to the corrective term of the diffusivity depending on the electrolyte concentration) has only minimal effects. Curves vary little also with the electrolyte composition; in particular, curves for Feed2 (0.5M seawater) and Feed3 (0.017M river water) are almost identical, while only the curve relative to Feed1 (5M brine) is slightly different (in particular, it starts from a higher value at low flow speed) because of the significantly different physical properties of this solution (e.g. liquid viscosity, Table 2).

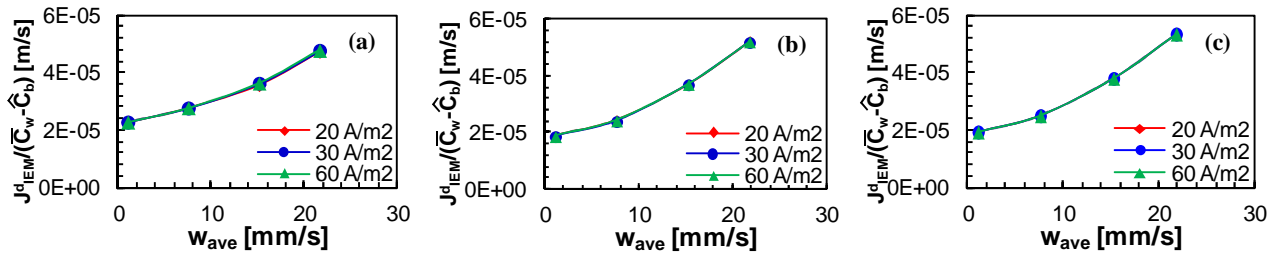


**Figure 10.** Ratio  $J_{IEM}^d / (\bar{C}_w - \hat{C}_b)$  as a function of fluid velocity for the D0 spacer-filled channel fed by (a) Feed1 (5M brine), (b) Feed2 (0.5M seawater) and (c) Feed3 (0.017M river water) at various current densities.

In accordance with the Nernst equation, in Reverse Electrodialysis systems, (as better discussed below), the driving force of the process depends on the ratio (and not on the difference) of the concentrations of the two solutions in contact with the membrane. Therefore, notwithstanding very similar values of  $\bar{C}_w - \hat{C}_b$  were found for the three feed concentrations, these led to very different effects on driving force. In this regard, it is useful to employ the polarization factor as defined in eqs. (14) and (15) to quantify polarization phenomena effect. Figure 11 shows the polarization factor as a function of the mean fluid velocity along the main flow direction. The polarization factor

is always close to one ( $\theta > 0.96$ ) when either Feed1 (5M brine) or Feed2 (0.5M seawater) are simulated, whereas it is significantly lower ( $\theta \approx 0.5\div 0.9$ ) for the case of Feed3 (0.017M river water). Therefore, at a given flow rate and current density, the higher the mean concentration of the feed solution, the higher the polarization factor. Also, the higher the current density (i.e. the higher the flux imposed at the membranes), the lower the value of  $\theta$ , although such a dependence is crucial only in the case of Feed3 (0.017M river water). Eventually, Figure 11 shows that a higher flow rate of the feed solution corresponds to an enhanced mixing within the channel leading polarization phenomena to decrease. The present findings confirm that polarization phenomena can be reduced by carefully optimizing the fluid dynamics within the stack.

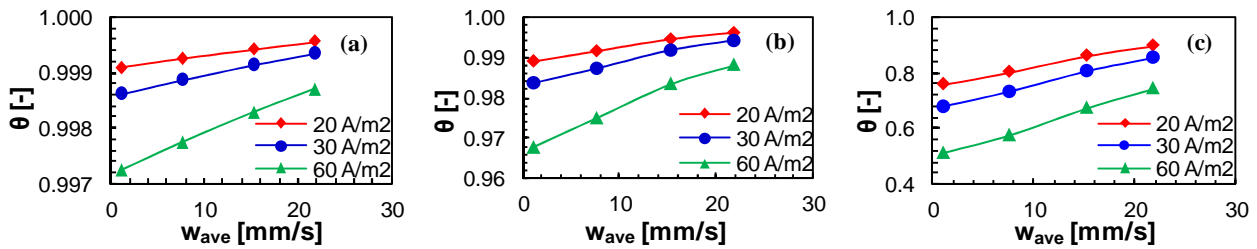


**Figure 11.** Polarization factor as a function of fluid velocity for the D0 spacer-filled channel fed by (a) Feed1 (5M brine), (b) Feed2 (0.5M seawater) and (c) Feed3 (0.017M river water) at various current densities.

The cell potential available in actual operating conditions is lower than the open circuit voltage. Following Vermaas et al. [19], the potential drop across a cell pair can be written as the sum of Ohmic resistances and two non-Ohmic voltage drops, as expressed by the following equation

$$U = E_{OCV} - \eta_{\Delta C} - \eta_{BL} - iR_{ohm} \quad (19)$$

where  $U$  is the voltage achievable over a cell pair,  $E_{OCV}$  is the open circuit voltage over the same cell pair,  $\eta_{\Delta C}$  is a loss of voltage due to the streamwise concentration change (i.e. along the compartment length) in the bulk of the solution,  $\eta_{BL}$  is a loss of voltage due to the concentration polarization in the boundary layers,  $i$  is the current density,  $R_{ohm}$  is the standard cell pair Ohmic

areal resistance. Therefore the quantity  $E_{OCV} - \eta_{BL}$  indicates how much polarization phenomena affect the obtainable potential by reducing  $E_{OCV}$ .

For the case of a monovalent binary electrolyte, considering the standard Nernst equation and assuming that the mean activity on the two interfaces of a channel are equal, this “corrected” potential in a cell pair can be estimated as:

$$E_{OCV} - \eta_{BL} = 2\alpha_m \frac{RT}{F} \left[ \ln \left( \frac{\hat{C}_b^{conc}}{\hat{C}_b^{dil}} \right) + \ln \left( \theta^{conc} \theta^{dil} \right) + \ln \left( \frac{\bar{\gamma}_w^{conc}}{\bar{\gamma}_w^{dil}} \right) \right] \quad (20)$$

where  $\alpha_m$  is the mean permselectivity of the ionic exchange membranes,  $\hat{C}_b$  is the bulk concentration of the electrolyte,  $\bar{\gamma}_w$  is the activity coefficient averaged over the plane corresponding to the membrane-solution interface,  $\theta$  is the polarization factor as defined by eqs. (14) and (15), the superscripts *conc* and *dil* refer to the concentrated and diluted channel respectively.

Figure 12a reports as functions of the average fluid velocity  $w_{ave}$  the quantity  $E_{OCV} - \eta_{BL}$ , calculated by eq. (20), for the D0 spacer,  $i = 60 \text{ A/m}^2$  and two electrolyte couples: (i) Feed1-Feed2 (brine-seawater, *BS*) and (ii) Feed2-Feed3 (seawater-river water, *SR*). The mean permselectivities were assumed to be  $\alpha_{m,BS} = 0.775$  and  $\alpha_{m,SR} = 0.96$  [39] and the temperature  $T = 298 \text{ K}$ . The activity coefficients are calculated on the basis of the Pitzer equation [40]. The uncorrected  $E_{OCV}$  is also reported for comparison purposes and, of course, does not vary with  $w_{ave}$ . These results show that (i)  $E_{OCV}$  is larger for *SR* than for *BS*; (ii) the voltage drop  $\eta_{BL}$  due to polarization effects is larger for *SR* than for *BS*; and (iii) the corrected voltage over a cell pair  $E_{OCV} - \eta_{BL}$  is higher for *SR* than for *BS* (up to 25% in the range of  $w_{ave}$  investigated). This is due to the higher bulk concentrations ratio and mean permselectivity for *SR* conditions. On the other hand, however, the term  $\ln \left( \bar{\gamma}_w^{conc} / \bar{\gamma}_w^{dil} \right)$  corresponds to a potential enhancement only in the case of *BS* conditions, where there is also a negligible effect of polarization phenomena, while it represents a detrimental contribution for *SR*

conditions. Finally, it should be stressed that higher power densities are obtained under *BS* conditions because of the much lower resistance of the dilute solution, as confirmed by results obtained by multi-scale modelling simulation [27].

Although quantitative comparisons with experimental data are not currently possible, it may be interesting to compare the present results on a qualitative and order-of-magnitude basis with chronopotentiometry results obtained by Vermaas et al. for similar solutions, geometries and spacers [8]. For example, for the *SR* electrolyte couple flowing in channels of height  $H = 200 \mu\text{m}$  equipped with commercial Sefar 03-300/51 net spacers, Vermaas et al. report a boundary layer areal resistance of  $\sim 7.5 \Omega \text{ cm}^2$  at  $w_{ave} = 5 \text{ mm/s}$  and  $\sim 5 \Omega \text{ cm}^2$  at  $w_{ave} = 20 \text{ mm/s}$ . Figure 12a shows that the boundary layer voltage drop  $\eta_{BL}$  for the *SR* couple in channels of a similar height ( $H=280 \mu\text{m}$ ) equipped with comparable D0 spacers under a current density  $i=60 \text{ A/m}^2$  is  $\sim 0.03 \text{ V}$  at  $w_{ave} = 5 \text{ mm/s}$  and  $\sim 0.015 \text{ V}$  at  $w_{ave} = 20 \text{ mm/s}$ . The corresponding  $R_{BL}$  are  $5 \Omega \text{ cm}^2$  and  $2.5 \Omega \text{ cm}^2$ , respectively, values which are at least of the correct order of magnitude.

A boundary layer efficiency can be defined as

$$\chi_{BL} = \frac{E_{OCV} - \eta_{BL}}{E_{OCV}} = \frac{\ln\left(\frac{\hat{C}_b^{conc}}{\hat{C}_b^{dil}}\right) + \ln(\theta^{conc} \theta^{dil}) + \ln\left(\frac{\bar{\gamma}_w^{conc}}{\bar{\gamma}_w^{dil}}\right)}{\ln\left(\frac{\hat{C}_b^{conc}}{\hat{C}_b^{dil}}\right) + \ln\left(\frac{\bar{\gamma}_w^{conc}}{\bar{\gamma}_w^{dil}}\right)} \quad (21)$$

and is plotted in Figure 12b as a function of  $w_{ave}$  for the same cases. The relative reduction of  $E_{OCV}$  is negligible for *BS* at all the flow rates considered, while for *SR*, in which the low Feed3 concentration (0.017M) is present on the diluate side, there is a significant reduction of the voltage (up to  $\sim 25\%$ ); the beneficial effect of raising the flow velocity is evident for this case. Of course, since the physico-chemical parameters of the various solutions do not differ significantly, a larger relative importance of polarization (i.e., a low  $\chi_{BL}$ ) for dilute solutions is to be expected.

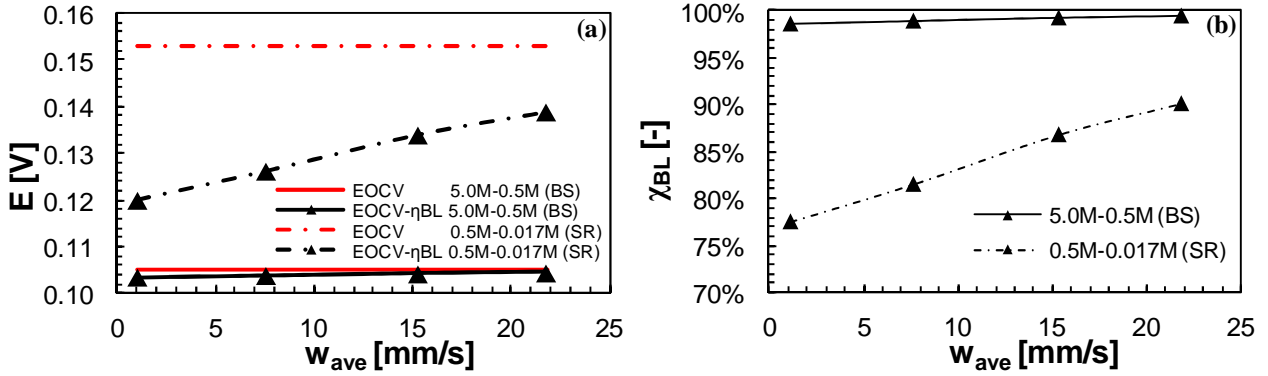


**Figure 12.** D0 spacer filled channel under Feed1-Feed2 (5M brine-0.5M seawater) and Feed2- Feed3 (0.5M seawater-0.017M river water) conditions at a current density  $i = 60 \text{ A/m}^2$ . (a) open circuit voltage (uncorrected and corrected for polarization effects); (b) boundary layer efficiency.

### 3.2 Comparison of different spacer geometries

The effect of spacer geometry and orientation on polarization phenomena was also investigated. As an example, Figure 13 shows concentration contours over the Unit Cell boundaries for all the configurations investigated here having Feed2 (0.5M seawater) as the dilute solution at a current density of  $200 \text{ A/m}^2$ . All cases are characterized by a pressure drop per unit length of  $0.01 \text{ bar/m}$  (imposed term  $K_p$  in eq. (16)), but differ in the mean flow speed  $w_{ave}$  and in the bulk Reynolds number  $Re$  due to the different geometry. Values of  $w_{ave}$  and  $Re$  are indicated besides each figure.

This figure shows that (i) the presence of the spacer strongly modify the concentration field compared to the spacer-less channel; (ii) not only the spacer geometry, but also its orientation can lead to completely different concentration fields; (iii) polarization is higher near the spacer wires where fluid velocities are allegedly lower; (iv) an angle of  $45^\circ$  between the spacer wires and the main fluid flow direction seems to provide lower concentration polarization.

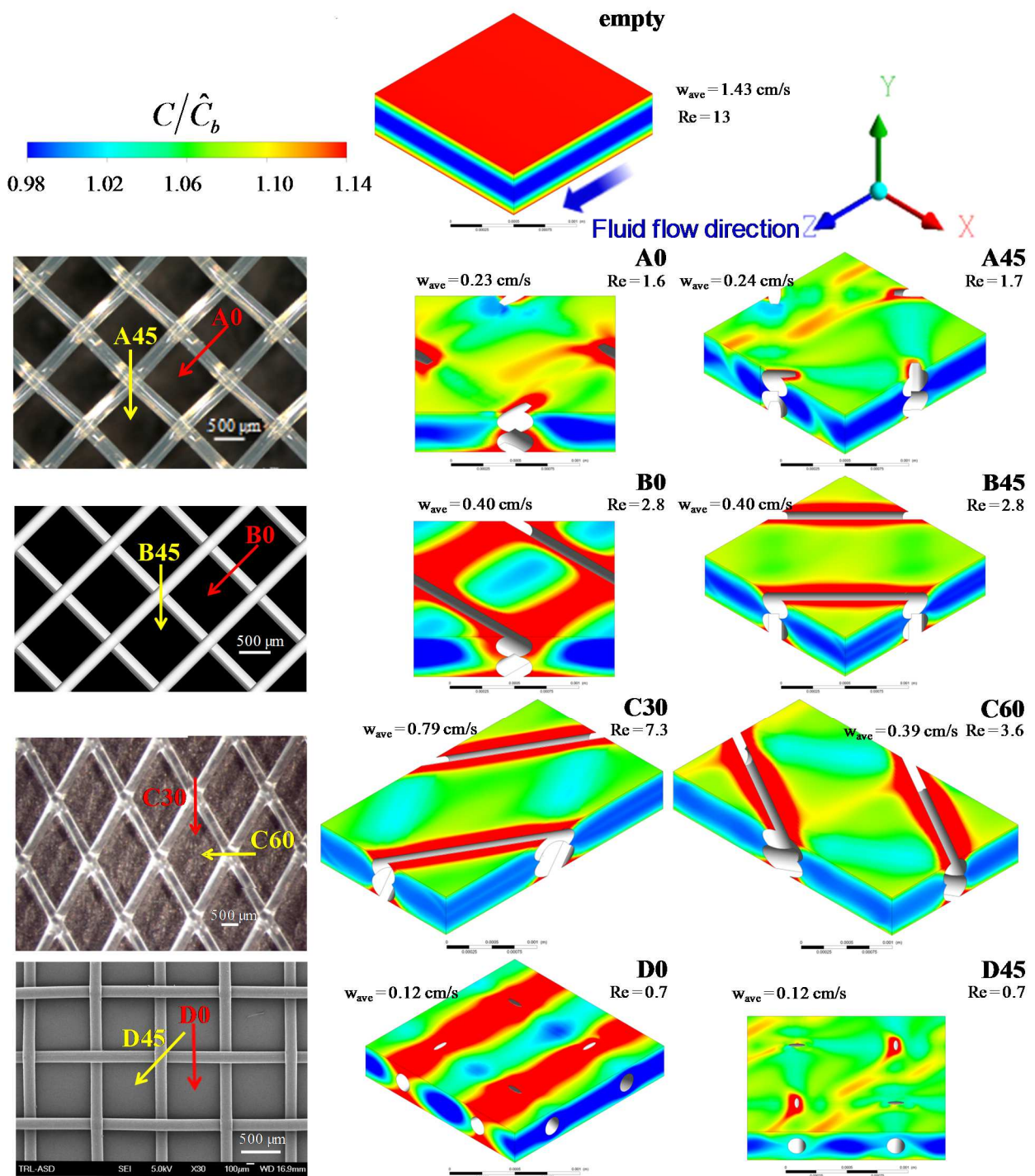


**Figure 13.** Normalized concentration distribution for empty channel, A0, A45, B0, B45, C30, C60, D0 and D45 spacer-filled channels fed by Feed2 (0.5M seawater) at a current density  $i = 200 \text{ A/m}^2$  and a pressure drop per unit length  $K_p = 0.01 \text{ bar/m}$ . The Reynolds numbers and mean fluid speed obtained are indicated besides each image.

The dependence of the Fanning friction factor on the Reynolds number was studied in order to better characterize the fluid dynamic behaviour of the spacer-filled channels under investigation.

The friction factor is defined as:

$$f = \frac{\Delta p}{l} \frac{d_{h,void}}{2\rho w_{mean,void}^2} \quad (22)$$

where  $d_{h,void}$  and  $w_{mean,void}$  are relevant to the empty channel corresponding to the spacer-filled one under consideration. In this way all the spacers are compared with respect to their reference empty channels, in order to highlight how each spacer modify fluid flow and transport features [38].

Results are reported in Figure 14. Clearly, the inclusion of any spacer leads the friction factor to strongly increase with respect to the spacer-less channel. No effect of the spacer orientation on the  $f-Re$  trend was found for the spacers A, B and D, whose angle between subsequent filaments is  $90^\circ$ .

In this regard, Shakaib et al. [41] found a difference of 12% in the pressure drops provided by two different orientation of a diamond spacer for Reynolds numbers quite higher than those investigated in the present work.

A different behaviour is exhibited by the two orientations of the spacer C whose angles between the filaments are of  $60^\circ$ - $120^\circ$ : the C30 orientation provided pressure losses far lower (about one half) than the configuration C60, because (i) in the C30 configuration the fluid encounters fewer filaments per unit length, and (ii) the lower angle between the main flow direction and the filaments results in a lower resistance to the flow [42]. We found a comparable behaviour in experiments involving similar but larger-scale spacers for membrane distillation [14]. Similar experimental findings were also reported by Da Costa et al. [43]. This large difference in pressure drops would have significant impact on the choice of the spacer orientation in commercial SGP-RE applications. As far as the comparison of the different spacers is concerned, the woven arrangement provides higher pressure drops than the overlapped one (see spacer A and B). Fumatech and Deukum spacers

(A and D respectively) have similar geometrical features, in particular they are woven spacers with a ratio mesh length/spacer length so similar that an analogous dependence of  $f$  on  $Re$  was found. Notwithstanding the spacer C60 is characterized by overlapped wires, it provides Fanning factors comparable to those provided by the woven spacers A and D. Conversely, the other configuration of the same spacer (i.e. C30) guarantees pressure losses lower than those provided by spacer B.

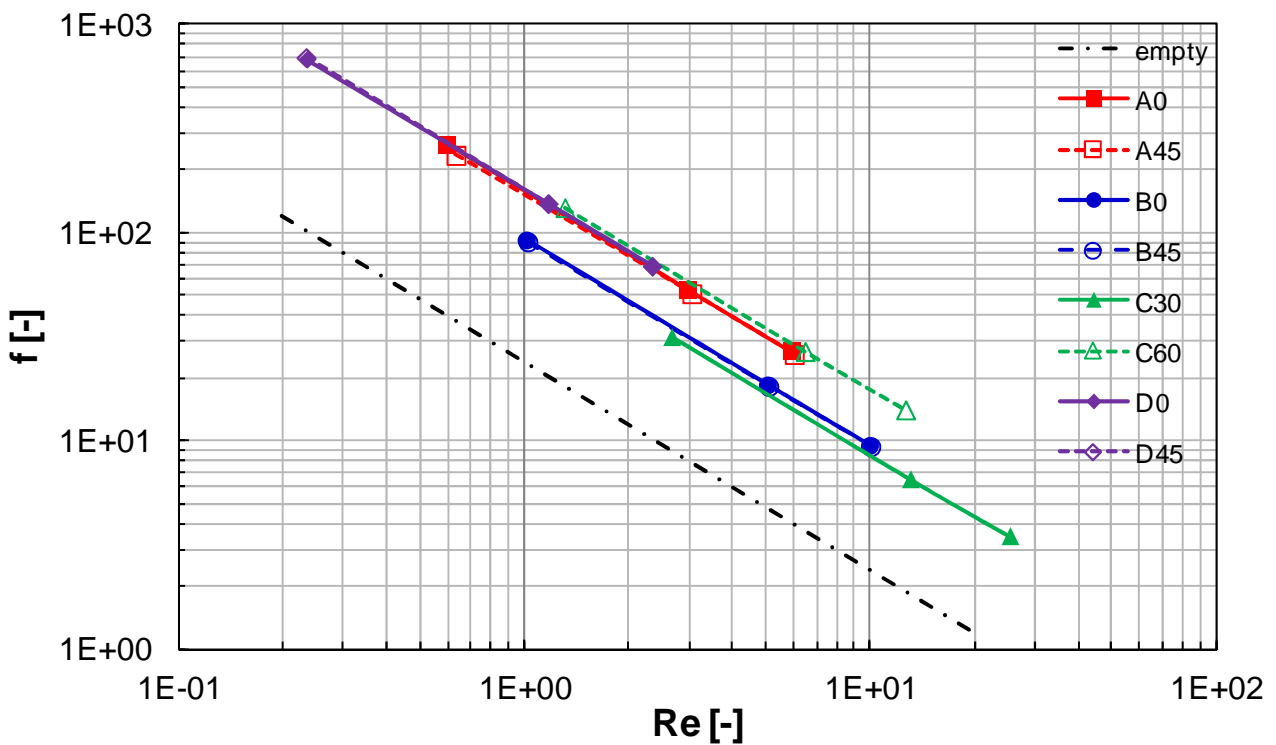


**Figure 14.** Fanning friction factor as a function of Reynolds number for all channels investigated, fed by Feed1.

Notably, for all the spacer-filled channels investigated  $f$  roughly shows a  $Re^{-1}$  trend, thus confirming the existence of a self-similar flow regime (creeping flow), at least at the lowest Reynolds numbers. Only at the highest  $Re$  (e.g. spacer C) some discrepancies from this trend can be observed. This occurrence is not due to turbulence (the Reynolds number is far too low for that, and the present numerical solutions gave perfectly steady-state results), but to a loss of self-similarity of the fluid flow field: the presence of the spacer causes secondary flows in the cross section of the channel

whose relative intensity increases with the flow rate. Such hypothesis is supported by evidence reported in Figure 15, where quite different normalized velocity distributions can be observed at two different Reynolds numbers for the case of the spacer configuration C30. This is the reason why a tenfold increase in the pressure drop per unit length leads to a slightly lower (~ninefold) increase in mean flow speed and Reynolds number (this last from 7.3 to 63.3), showing that the pressure drop increases more than linearly with the flow rate.

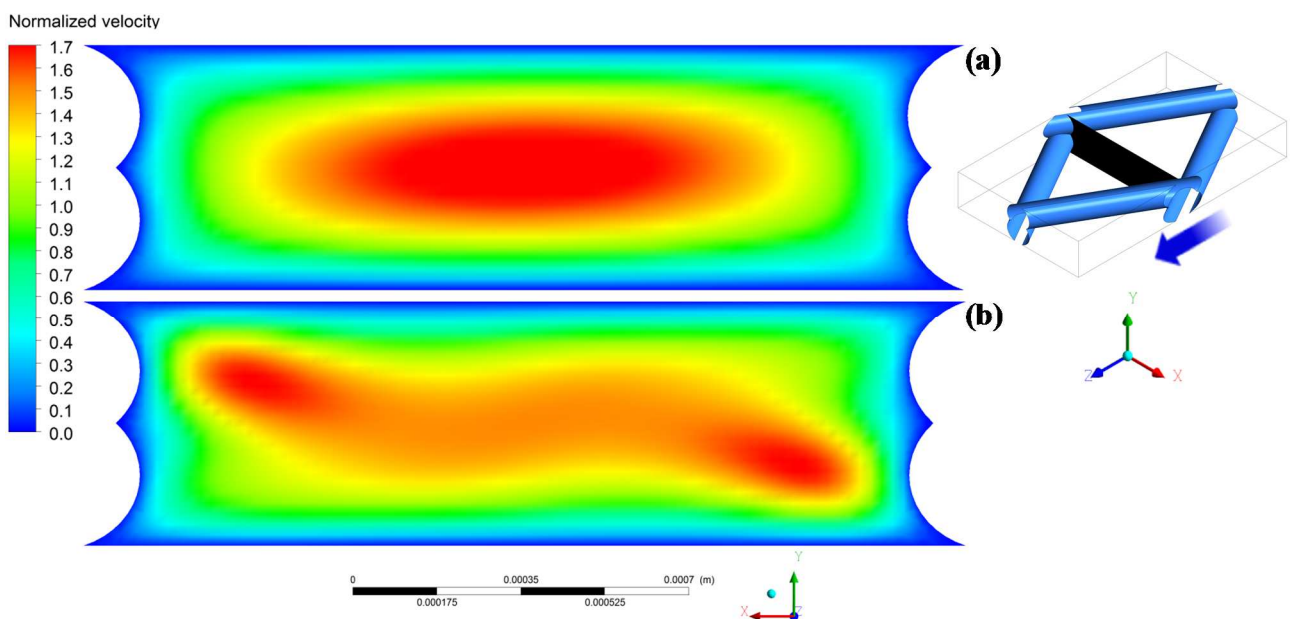


**Figure 15.** Normalized velocity maps on the  $x$ - $y$  middle plane, for the C30 spacer-filled channel fed by Feed2 at a pressure drop per unit length (a)  $K_p = 0.01$  bar/m ( $Re = 7.3$ ,  $w_{ave} = 0.79$  cm/s) and (b)  $K_p = 0.1$  bar/m ( $Re = 63.3$ ,  $w_{ave} = 6.89$  cm/s).

A quantitative comparison among the cases investigated in terms of concentration polarization is shown in Figure 16 which reports the polarization factor as a function of the Reynolds number. It shows all the channel configurations fed by Feed1 (5M brine) or Feed2 (0.5M seawater) at a current density of  $200 \text{ A/m}^2$ . In the empty channel  $\theta$  is constant with  $Re$ , because the flow is perfectly steady and parallel so that mixing does not occur and only the  $z$ -component of velocity is present. Conversely, as expected, a performance enhancement can be observed as  $Re$  increases (i.e. as inertial terms overcome viscous ones) when a spacer is included within the channel: its presence

produces velocity components perpendicular to the membrane surfaces, whose relative importance increases as the flow rate increases. Results of Figure 16 confirm what reported in literature on diamond spacers with overlapped filaments: (i) for the spacer B a mass transfer enhancement is obtained when the fluid flow direction bisects the angle between the filaments [41]; (ii) the configuration C60 leads to an improved mixing with respect to the configuration C30 [43].

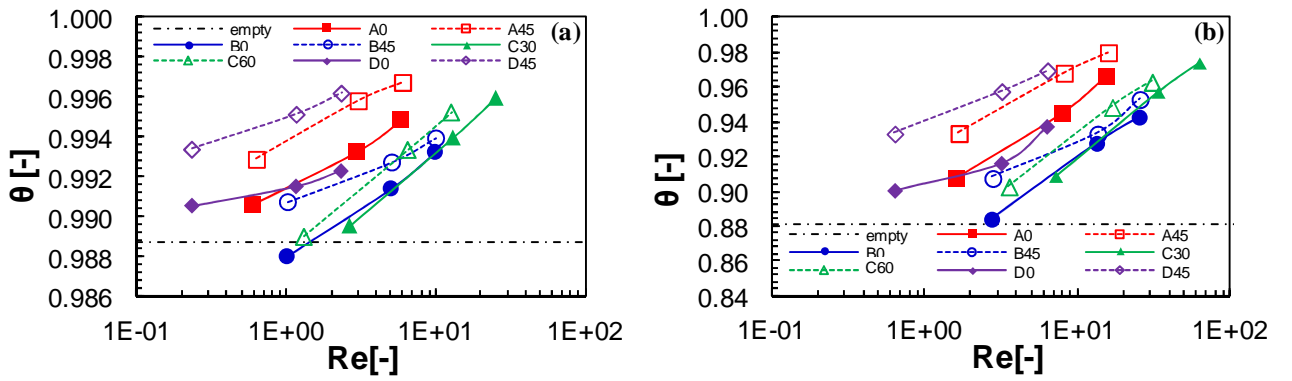


**Figure 16.** Polarization factor as a function of the Reynolds number for all channels investigated, fed by (a) Feed1 (5M brine) and (b) Feed2 (0.5M seawater) at a current density  $i = 200 \text{ A/m}^2$ .

However, referring to the pumping power consumption necessary to achieve a certain  $\theta$  value is the best way to suitably compare the various spacer performance and infer the process efficiency. In order to quantify such efficiency, various authors have adopted a dimensionless power number  $Pn$  [42, 44, 45] defined as

$$Pn = \text{SPC} \frac{\rho^2 H^4}{\mu^3} = \frac{1}{8} f Re^3 \quad (23)$$

where SPC is the specific power consumption

$$\text{SPC} = \frac{\Delta p}{l} w_{mean,void} \quad (24)$$

The polarization factor  $\theta$  as a function of the power number  $Pn$  for the investigated spacers is reported in Figure 17. Clearly, high  $\theta$  with low  $Pn$  is the preferable condition. Notably, this figure

concerns only Feed1 (5M brine) and Feed2 (0.5M seawater). Feed3 (0.017M river water) is not reported for brevity since very similar considerations can be inferred for the three feeds.

By comparing Figure 14 with Figure 17 some considerations can be made: notwithstanding the spacer orientation does not provide substantial differences in pressure drops (see spacers A, B and D) on the one hand, on the other hand it leads to very different polarization factors. In particular, spacer configurations with the flow attack angle of  $0^\circ$  provide  $\theta$  lower than those obtainable in the corresponding  $45^\circ$  configurations. This occurs because convection perpendicularly to the membranes is disadvantaged when the fluid is parallel to a filament array. Such findings are in accordance with those by Li et al. [44] and Shakaib et al. [41], although they studied only overlapped spacer at  $Pn$  values quite higher ( $>10^5$ ) than those investigated in the present work. As far as the filament array arrangement is concerned, results show that the woven spacers guarantee  $\theta$  higher than the overlapped ones at a given  $Pn$  value. This is not surprising since at the lowest flow rates investigated, the woven arrangement forces the whole fluid volume to move up and down continuously thus (i) providing significant velocity components perpendicular to the membranes and (ii) avoiding the presence of stagnant zones. Conversely, the overlapped arrangement at the lowest Reynolds numbers investigated here does not provide an efficient mixing since a part of the fluid move along the longitudinal filaments without practically encountering any obstacles, while many calm zones take place between the filaments perpendicular to the main flow direction. This occurrence explains why polarization factors lower than the one relevant to the empty channel can be obtained at the lowest flow rates. As regards spacer C, being an overlapped spacer it generally provides low  $\theta$  values. When the two different orientations of this spacer are compared, one may observe that the higher pressure drops provided by C60 (Figure 14) at any given  $Re$  are counterbalanced by the higher  $\theta$  (Figure 16).

Finally, results of Figure 17 confirm that polarization effect is negligible when Feed1 (brine) is flowing in the channel even at very high current densities and low flow rates. In the case of Feed2 (seawater), concentration polarization effect is still very low but of higher significance, while for less concentrated solutions it can play a key role (see Figure 11). These findings suggest that, when concentrated solutions are adopted, the channel geometry should be optimized taking into account other aspects such as pressure drop, residence time, electrical resistance, etc. Conversely, when diluted solutions are employed, a proper attention should be paid to polarization phenomena effects which can dramatically affect the driving force and thus the efficiency of the process. In such cases, a woven arrangement and a flow attack angle of  $45^\circ$  appears to be the best performing configuration for a spacer-filled channel in high efficiency (high current densities) Reverse Electrodialysis applications, among those presently investigated.

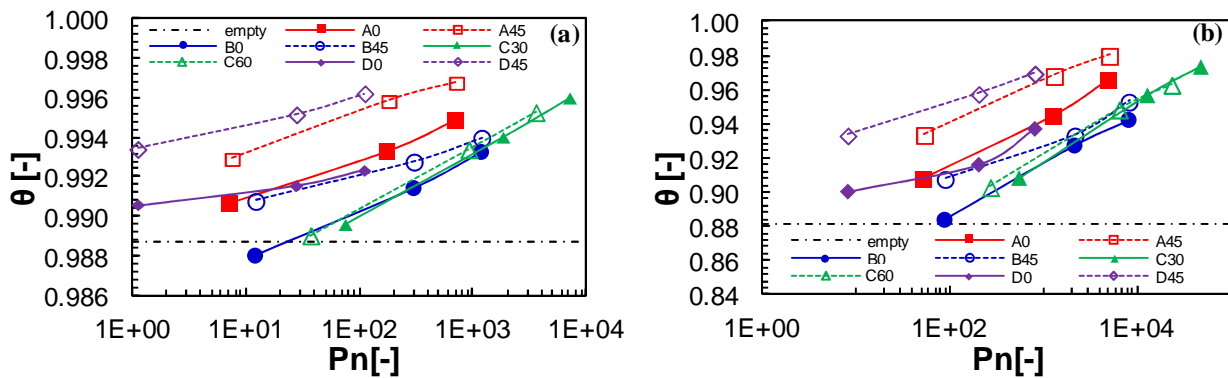


**Figure 17.** Polarization factor as a function of pressure drop for all channels investigated, fed by (a) Feed1 and (b) Feed2 at a current density  $i = 200 \text{ A/m}^2$ .

#### 4 Conclusions

A CFD model was developed in order to study concentration polarization phenomena in Reverse Electrodialysis channels. A transport equation suitable also for concentrated solutions was implemented in the CFD code Ansys® CFX 13. A Unit Cell approach was used, based on inlet-outlet periodicity of velocity, pressure and concentration and valid for fully developed conditions.

The concentration field was found to be greatly controlled by the diffusive transport, while the migrative one had a negligible effect on results. The dependence of polarization phenomena on various parameters was thoroughly addressed:

- Polarization phenomena are slightly affected by the solution features, but polarization effects greatly decrease as the solution concentration increases. In particular, they are important for river water, barely significant for seawater, and practically negligible for brine.
- The higher the current density, the lower the polarization factor  $\theta$  (i.e. the higher the polarization effects). However, even at very high current densities stacks fed by brine and seawater do not exhibit significant polarization effects (especially on the brine side).
- Although the fluid flow regime was laminar for all cases investigated, fluid flow was found to strongly affect polarization phenomena. This is due to the non-similarity of the flow field at the various flow rates and to the presence of velocity components perpendicular to the membranes. Factors promoting fluid mixing within the channel (e.g. the presence of a net spacer and the increase of feed flow rate) were found to enhance the polarization factor, although, on the other hand, they also lead to increased pressure drops. Of course, no effect of flow rate on polarization phenomena was observed for the empty channel where no velocity component perpendicular to the membrane is present.
- As regards the spacer configuration, for the flow rates range investigated here, spacers with woven arrays of filaments were found to provide higher  $\theta$  at any given normalized pumping power  $Pn$  with respect to overlapped arrays. For any wire arrangement a flow attack angle of  $45^\circ$  results in more efficient mixing compared to the  $90^\circ$  case. Different angles between the filaments do not provide different  $\theta - Pn$  trends.

Finally, on the basis of all these findings it is worth observing that for the concentrated solutions feeds investigated here (which represent seawater and brine), where concentration polarization

effects do not appear to be crucial, other factors should drive the optimization strategy, such as the influence of channel thickness and geometry on the compartment Ohmic resistance, the pressure drop, the plugging potential within the channel and the residence time in the stack.

A limitation of the results presented here is that – for the time being – they lack a proper validation against experimental data. Unfortunately, the current state of the art in Reverse Electrodialysis experiments is not such that a quantitative validation of simulation results like the present ones can be hoped for. This is partly due to this being a young field: the resources dedicated to it so far are not very large, and often the investigators have focused on general system performance and not on individual effects such as concentration polarization. Polarization losses are inevitably superimposed to (often larger) Ohmic losses both in the fluids and in the membranes and to other sources of irreversibility, which makes their assessment a difficult task requiring focused investigations. Hopefully, these will become available in the near future.

All the results and conclusions presented should be regarded as a way to obtain some important preliminary insights on the optimization of SGP-RE systems (including also fluid dynamics and mass transfer aspects) while a more thoroughly optimization study involving also the other phenomena will be matter for future work.

### **Acknowledgement**

This work was performed within the REAPower (Reverse Electrodialysis Alternative Power production) project (<http://www.reapower.eu>) funded by the EU-FP7 programme (Project Number: 256736).

## Notation

$a$	Slope of the function $\rho(C)$ obtained via linear regression in the proximity of the bulk concentration [ $\text{kg mol}^{-1}$ ]
$A$	Membrane surface area in a Unit Cell [ $\text{m}^2$ ]
$b$	Intercept of the function $\rho(C)$ obtained via linear regression in the proximity of the bulk concentration [ $\text{kg m}^{-3}$ ]
$C$	Molar concentration of electrolyte [ $\text{mol m}^{-3}$ ]
$\tilde{C}$	Periodic molar concentration of electrolyte [ $\text{mol m}^{-3}$ ]
$\hat{C}_b$	Bulk concentration of electrolyte [ $\text{mol m}^{-3}$ ]
$C_i$	Concentration of species $i$ [ $\text{mol m}^{-3}$ ]
$C_w$	Molar concentration of electrolyte at membrane-solution interface [ $\text{mol m}^{-3}$ ]
$\bar{C}_w$	Mean molar concentration of electrolyte at membrane-solution interface [ $\text{mol m}^{-3}$ ]
$D$	Measured diffusion coefficient of electrolyte [ $\text{m}^2 \text{s}^{-1}$ ]
$d_{h,void}$	Hydraulic diameter of the spacer-less channel [m]
$E_{ocv}$	Open circuit voltage over a cell pair [V]
$f$	Fanning friction factor [-]
$F$	Faraday's constant [ $\text{C mol}^{-1}$ ]
$H$	Channel thickness [m]
$\bar{i}$	Current density [ $\text{A m}^{-2}$ ]
$\bar{J}_i^m$	Migrative flux of species $i$ [ $\text{mol m}^{-2} \text{s}^{-1}$ ]
$\bar{J}_{co,IEM}^d$	Diffusive flux of co-ion at the membrane-solution interface [ $\text{mol m}^{-2} \text{s}^{-1}$ ]
$\bar{J}_{IEM}^d$	Diffusive flux of electrolyte at membrane-solution interface [ $\text{mol m}^{-2} \text{s}^{-1}$ ]
$\bar{J}_{IEM}^d$	Mean diffusive flux through the membranes [ $\text{mol m}^{-2} \text{s}^{-1}$ ]
$\vec{k}$	Unit vector of the $z$ axis [-]
$K_c$	Concentration gradient along the main flow direction [ $\text{mol m}^{-4}$ ]
$K_p$	Pressure gradient along the main flow direction [ $\text{N m}^{-3}$ ]
$M_e$	Molar mass of electrolyte [ $\text{kg mol}^{-1}$ ]
$p$	Pressure [Pa]
$\tilde{p}$	Periodic pressure [Pa]
$Pn$	Power number [-]
$R$	Universal gas constant [ $\text{J mol}^{-1} \text{K}^{-1}$ ]
$R_{BL}$	Boundary layer areal resistance [ $\Omega \text{m}^{-2}$ ]
$Re$	Reynolds number [-]
$R_{ohm}$	Ohmic area resistance over a cell pair [ $\Omega \text{m}^2$ ]
SPC	Specific power consumption [ $\text{Pa s}^{-1}$ ]
$t$	Time [s]
$T$	Absolute temperature [K]

$t_i^0$	Transference number of species $i$ with respect to the solvent velocity [-]
$U$	Voltage achievable over a cell pair [V]
$\vec{u}$	Velocity of solution [ $\text{m s}^{-1}$ ]
$V$	Volume of a Unit Cell [ $\text{m}^3$ ]
$w$	Velocity component along the flow direction $z$ [ $\text{m s}^{-1}$ ]
$w_{mean,void}$	Average velocity along $z$ in a corresponding spacerless channel [ $\text{m s}^{-1}$ ]
$x, y, z$	Cartesian coordinates [m]
$z_i$	Charge number of ionic species $i$ [-]

### ***Greek letters***

$\alpha_m$	Mean permselectivity of the ionic exchange membranes [-]
$\bar{\gamma}_w$	Mean molal activity coefficient of electrolyte averaged over membrane-solution interface [ $\text{mol m}^{-3}$ ]
$\eta_{BL}$	Loss of voltage over a cell pair due to the boundary layer [V]
$\eta_{\Delta C}$	Loss of voltage over a cell pair due to the streamwise concentration change [V]
$\theta$	Polarization factor [-]
$\mu$	Dynamic viscosity of solution [Pa s]
$\nu_i$	Stoichiometric coefficient of ionic species $i$
$\rho$	Density of solution [ $\text{kg m}^{-3}$ ]
$\chi_{BL}$	Boundary layer efficiency [-]

### ***Subscripts***

$0$	Solvent
$AEM$	Anionic exchange membrane-solution interface
$ave$	Average value in the fluid domain
$b$	Bulk
$CEM$	Cationic exchange membrane-solution interface
$co$	Co-ion
$i$	Species $i$
$IEM$	Ionic exchange membrane-solution interface
$w$	Membrane-solution interface (wall)
$+$	Cation
$-$	Anion

### *Superscripts*

<i>conc</i>	Concentrated
<i>d</i>	Diffusive
<i>dil</i>	Diluate
<i>m</i>	Migrative
<i>tot</i>	Total

### *Abbreviations*

<i>BS</i>	Brine-Seawater
<i>CFD</i>	Computational Fluid Dynamics
<i>IEM</i>	Ionic Exchange Membrane
<i>RE</i>	Reverse Electrodialysis
<i>SGP-RE</i>	Salinity Gradient Power-Reverse Electrodialysis
<i>SR</i>	Seawater-River water

### **References**

- [1] R.E. Pattle, Production of Electric Power by mixing Fresh and Salt Water in Hydroelectric Pile, *Nature*, 174 (1954) 660.
- [2] P. Długołęcki, K. Nijmeijer, S.J. Metz, M. Wessling, Current status of ion exchange membranes for power generation from salinity gradients, *J. Membr. Sci.*, 319 (2008) 214-222.
- [3] J.W. Post, H.V.M. Hamelers, C.J.N. Buisman, Energy Recovery from Controlled Mixing Salt and Fresh Water with a Reverse Electrodialysis System, *Environ. Sci. Technol.*, 42 (2008) 5785-5790.
- [4] J. Veerman, M. Saakes, S.J. Metz, G.J. Harmsen, Reverse electrodialysis: Performance of a stack with 50 cells on the mixing of sea and river water, *J. Membr. Sci.*, 327 (2009) 136-144.
- [5] O. Scialdone, A. Albanese, A. D'Angelo, A. Galia, C. Guarisco, Investigation of electrode material - Redox couple systems for reverse electrodialysis processes. Part II: Experiments in a stack with 10-50 cell pairs, *J. Electroanal. Chem.*, 704 (2013) 1-9.
- [6] O. Scialdone, C. Guarisco, S. Grispo, A. D'Angelo, A. Galia, Investigation of electrode material - Redox couple systems for reverse electrodialysis processes. Part I: Iron redox couples, *J. Electroanal. Chem.*, 681 (2012) 66-75.
- [7] A. Tamburini, G. La Barbera, A. Cipollina, M. Ciofalo, G. Micale, CFD simulation of channels for direct and reverse electrodialysis, *Desalination and Water Treatment*, 48 (2012) 370-389.
- [8] D.A. Vermaas, M. Saakes, K. Nijmeijer, Doubled Power Density from Salinity Gradients at Reduced Intermembrane Distance, *Environ. Sci. Technol.*, 45 (2011) 7089-7095.
- [9] A. Cipollina, M.G. Di Sparti, A. Tamburini, G. Micale, Development of a Membrane Distillation module for solar energy seawater desalination, *Chem. Eng. Res. Des.*, 90 (2012) 2101-2121.

- [10] V. Geraldes, V. Semião, M.N. Pinho, Hydrodynamics and concentration polarization in NF/RO spiral-wound modules with ladder-type spacers, *Desalination*, 157 (2003) 395-402.
- [11] E. Nagy, E. Kulcsára, A. Nagy, Membrane mass transport by nanofiltration: Coupled effect of the polarization and membrane layers, *J. Membr. Sci.*, 368 (2011) 215-222.
- [12] S.S. Sablani, M.F.A. Goosen, R. Al-Belushi, M. Wilf, Concentration polarization in ultrafiltration and reverse osmosis: a critical review, *Desalination*, 141 (2001) 269-289.
- [13] A. Tamburini, G. Micale, M. Ciofalo, A. Cipollina, Experimental analysis via Thermochromic Liquid Crystals of the temperature local distribution in Membrane Distillation modules, *Chemical Engineering Transactions*, 32 (2013) 2041-2046.
- [14] A. Tamburini, P. Pitò, A. Cipollina, G. Micale, M. Ciofalo, A Thermochromic Liquid Crystals image analysis technique to investigate temperature polarization in spacer-filled channels for membrane distillation, *J. Membr. Sci.*, 447 (2013) 260-273.
- [15] S. Wardeh, H.P. Morvan, CFD simulations of flow and concentration polarization in spacer-filled channels for application to water desalination, *Chem. Eng. Res. Des.*, 86 (2008) 1107-1116.
- [16] H. Strathmann, *Ion-exchange membrane separation processes*, first ed., Elsevier, Amsterdam, 2004.
- [17] E. Brauns, Salinity gradient power by reverse electro dialysis: effect of model parameters on electrical power output, *Desalination*, 237 (2009) 378-391.
- [18] D.A. Vermaas, M. Saakes, K. Nijmeijer, Power generation using profiled membranes in reverse electro dialysis, *J. Membr. Sci.*, 385-386 (2011) 234-242.
- [19] D.A. Vermaas, E. Guler, M. Saakes, K. Nijmeijer, Theoretical power density from salinity gradients using reverse electro dialysis, *Energy Procedia*, 20 (2012) 170-184.
- [20] P. Długołęcki, P. Ogonowski, S.J. Metz, M. Saakes, K. Nijmeijer, M. Wessling, On the resistances of membrane, diffusion boundary layer and double layer in ion exchange membrane transport, *J. Membr. Sci.*, 349 (2010) 369-379.
- [21] P. Długołęcki, A. Gambier, K. Nijmeijer, M. M. Wessling, Practical Potential of Reverse Electro dialysis As Process for Sustainable Energy Generation, *Environ. Sci. Technol.*, 43 (2009) 6888-6894.
- [22] R.E. Lacey, Energy by reverse electro dialysis, *Ocean Eng.*, 7 (1980) 1-47.
- [23] E. Brauns, Finite elements-based 2D theoretical analysis of the effect of IEX membrane thickness and salt solution residence time on the ion transport within a salinity gradient power reverse electro dialysis half cell pair, *Desalination and Water Treatment*, 51 (2013) 6429-6443.
- [24] L. Gurreri, A. Tamburini, A. Cipollina, G. Micale, M. Ciofalo, CFD simulation of mass transfer phenomena in spacer filled channels for reverse electro dialysis applications, *Chemical Engineering Transactions*, 32 (2013) 1879-1884.
- [25] E. Brauns, Towards a worldwide sustainable and simultaneous large scale production of renewable energy and potable water through salinity gradient power by combining reversal electro dialysis and solar power?, *Desalination*, 219 (2008) 312-323.
- [26] E. Brauns, An alternative hybrid concept combining seawater desalination, solar energy and reverse electro dialysis for a sustainable production of sweet water and electrical energy, *Desalination and Water Treatment*, 13 (2010) 53-62.

- [27] M. Tedesco, A. Cipollina, A. Tamburini, G. Micale, J. Helsen, M. Papapetrou, Reapower - Use of desalination brine for power production through reverse electro dialysis, *Desalination and Water Treatment*, accepted for publication (2014).
- [28] D.W. Green, R.H. Perry, *Perry's Chemical Engineers' Handbook*, eighth ed., McGraw-Hill, New York, 2007.
- [29] H. Ozbek, J.A. Fair, S.L. Phillips, Viscosity Of Aqueous Sodium Chloride Solutions From 0 - 150°C, in, University of California, Berkeley, 2010.
- [30] V. Vitagliano, P.A. Lyons, Diffusion Coefficients for Aqueous Solutions of Sodium Chloride and Barium Chloride, *J. Am. Chem. Soc.*, 78 (1956) 1549-1552.
- [31] J.S. Newman, *Electrochemical Systems*, Prentice Hall, 1991.
- [32] L.J.M. Smits, E.M. Duyvis, Transport Numbers of Concentrated Sodium Chloride Solutions at 25°, *J. Phys. Chem.*, 70 (1966) 2747-2753.
- [33] M. Ciofalo, J. Stasiek, M.W. Collins, Investigation of flow and heat transfer in corrugated passages - II. Numerical simulations, *Int. J. Heat Mass Transf.*, 39 (1996) 165-192.
- [34] L. Gurreri, A. Tamburini, A. Cipollina, G. Micale, CFD analysis of the fluid flow behavior in a reverse electro dialysis stack, *Desalination and Water Treatment*, 48 (2012) 390-403.
- [35] C.P. Koutsou, S.G. Yiantsios, A.J. Karabelas, Direct numerical simulation of flow in spacer-filled channels: Effect of spacer geometrical characteristics, *J. Membr. Sci.*, 291 (2007) 53-69.
- [36] Y.L. Li, K.L. Tung, CFD simulation of fluid flow through spacer-filled membrane module: selecting suitable cell types for periodic boundary conditions, *Desalination*, 233 (2008) 351-358.
- [37] A. Tamburini, G. La Barbera, A. Cipollina, G. Micale, M. Ciofalo, CFD prediction of scalar transport in thin channels for reverse electro dialysis, Submitted to *Desalination & Water Treatment*, (2013).
- [38] G. Schock, A. Miquel, Mass transfer and pressure loss in spiral wound modules, *Desalination*, 64 (1987) 339-352.
- [39] M. Tedesco, A. Cipollina, A. Tamburini, W. van Baak, G. Micale, Modelling the Reverse ElectroDialysis process with seawater and concentrated brines, *Desalination and Water Treatment*, 49 (2012) 404-424.
- [40] K.S. Pitzer, Thermodynamics of electrolytes. I. Theoretical basis and general equations, *J. Phys. Chem.*, 77 (1973) 268-277.
- [41] M. Shakaib, S.M.F. Hasani, M. Mahmood, CFD modeling for flow and mass transfer in spacer-obstructed membrane feed channels, *J. Membr. Sci.*, 326 (2009) 270-284.
- [42] M. Shakaib, S.M.F. Hasani, M. Mahmood, Study on the effects of spacer geometry in membrane feed channels using three-dimensional computational flow modeling, *J. Membr. Sci.*, 297 (2007) 74-89.
- [43] A.R. Da Costa, A.G. Fane, D.E. Wiley, Spacer characterization and pressure drop modelling in spacer-filled channels for ultrafiltration, *J. Membr. Sci.*, 87 (1994) 79-98.
- [44] F. Li, W. Meindersma, A.B. de Haan, T. Reith, Optimization of commercial net spacers in spiral wound membrane modules, *J. Membr. Sci.*, 208 (2002) 289-302.
- [45] J. Liu, A. Iranshahi, Y. Lou, G. Lipscomb, Static mixing spacers for spiral wound modules, *J. Membr. Sci.*, 442 (2013) 140-148.